博士論文

半導体超格子における
電子－フォノン相互作用の理論

土家　琢磨
東京大学物性研究所

１９９０年１２月

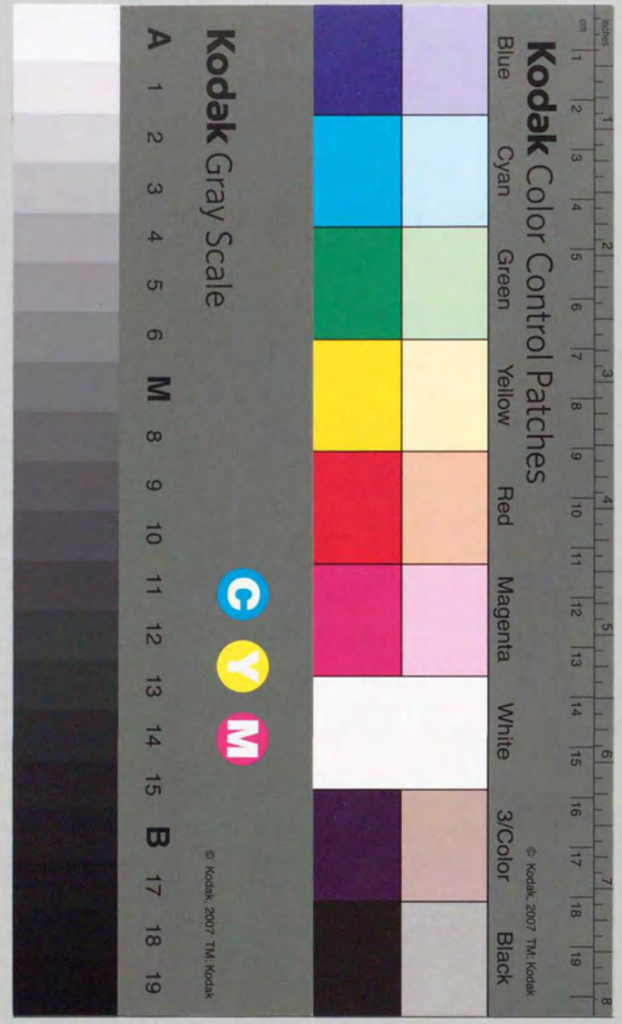

Thesis

Theory of Electron-Phonon Interaction in Semiconductor Superlattices

Takuma Tsuchiya

Institute for Solid-State Physics

University of Tokyo

December 1990

Acknowledgements

The author would like to express his sincerest gratitude to Professor Tsuneya Ando for his continual guidance and encouragement throughout the course of the present work and critical reading of the manuscript. He indebted to Dr. Hiroshi Akera for useful advice and valuable discussions. He is grateful to Dr. Gerrit E.W. Bauer for critical reading of the manuscript. He wishes to thank Professor Shin'ichi Katayama for helpful discussions in early stage of this work. He is also pleased to acknowledge continual encouragement by Professor Hidetoshi Fukuyama and Mrs. Shizue Maruyama. Many interesting conversations with all members of the research groups under Professor T. Ando and Professor H. Fukuyama are also acknowledged.

The author dedicates this thesis to his parents to express his gratitude for many years of upbringing and encouragements.

Contents

Chapter 1

Introduction

Since the prediction of negative differential conductivity and Bloch oscillations due to the negative mass effect in semiconductor superlattices by Esaki and Tsu in 1970,[1] the properties of semiconductor heterostructures have been one of the most important subjects in solid state physics for about twenty years. Schematic band diagrams of these structures are shown in Fig. 1. Molecular beam epitaxy (MBE) and liquid phase epitaxy were thought to be suitable for synthesis of these structures. In 1976, it was confirmed by X-ray diffraction,[2] transmission electron microscopy, and the electron beam diffraction[3] that superlattices can be made by MBE. Later, superlattices with good quality were made also by the metal-organic chemical-vapor-deposition. Among various combinations of different materials, the $GaAs/Al_xGa_{1-x}As$ system is most studied up to now.

Optical experiments are the most powerful method to investigate the electronic structure of semiconductors. Generally, in quasi-two-dimensional structures, such as inversion layers in silicon metal-oxide-semiconductor (MOS) structures, quantum levels due to the confinement of carriers are formed and the density of states becomes a step like function of energy. Quantized energy levels are expected also in the present structures. Figure 2 shows absorption spectra of $Al_{0.2}Ga_{0.8}As/GaAs/Al_{0.2}Ga_{0.8}As$ multiple quantum wells, constructed by piling up many single quantum wells, observed at 2K by Dingle *et al.*[4] The spectra are

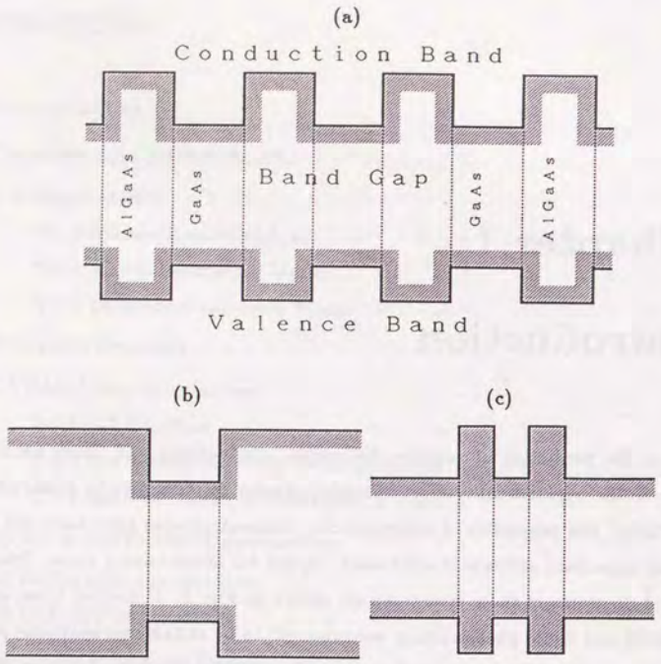

Figure 1 Schematic energy diagram of (a) a $GaAs/Al_xGa_{1-x}As$ superlattice, (b) a single quantum well or a double heterostructure, and (c) a double-barrier structure. The hatched area is the gap between the bottom of the conduction band and the top of the valence band.

strongly modified by the effect of exciton peaks and the subband edges are just above the exciton peak energies.

The lineup of bands at heterointerfaces, which determines the height of the potential barriers for electrons and holes, is important for device applications based on this system and also interesting from the point of view of physics. For the $GaAs/Al_xGa_{1-x}As$ systems, we characterize this lineup in terms of $\Delta E_c/\Delta E_v$, where ΔE_c is the discontinuity of the bottom of the conduction band at the interface and ΔE_v is that of the top of the valence band. The band discontinuity can

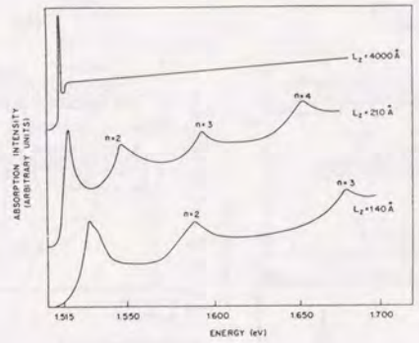

Figure 2 Absorption spectra of $Al_{0.2}Ga_{0.8}As/GaAs/Al_{0.2}Ga_{0.8}As$ multiple quantum wells observed by Dingle *et al.*[4] L_z is the thickness of the GaAs layer and n is the subband index.

be determined, for example, by a detailed analysis of absorption spectra. Dingle *et al.*[4] determined the ratio to be 85%/15% in 1974 for the first time, using the absorption spectra given in Fig. 2. This value was believed for ten years. In 1984, Miller *et al.*[5] claimed that the ratio is much smaller than 85%/15% based on photoluminescence spectra of $Al_xGa_{1-x}As$ parabolic quantum wells grown in such a way that the potential varies parabolically. The determination of the correct value is difficult because it requires the accurate knowledge of the band structure of the valence band, particularly the effective mass of a hole, which depends on various parameters of quantum wells, such as the thickness, the Al composition, and so on. As a result of extensive studies including those based on other methods such as XPS, C-V profiling, *etc.*, it is now believed that the ratio is about 60%/40%.

The average thickness of each layer in superlattices can be accurately controlled by growth times and RHEED oscillation. However, its local thickness can fluctuate from place to place as shown in Figs. 3(a) and 3(b), because of roughness or growth islands at heterointerfaces. This fluctuation can be observed indirectly through photoluminescence spectra.[7,6] In Figs. 3(c) and 3(d), photoluminescence spectra of two samples with four quantum wells with different thickness are shown.[6]

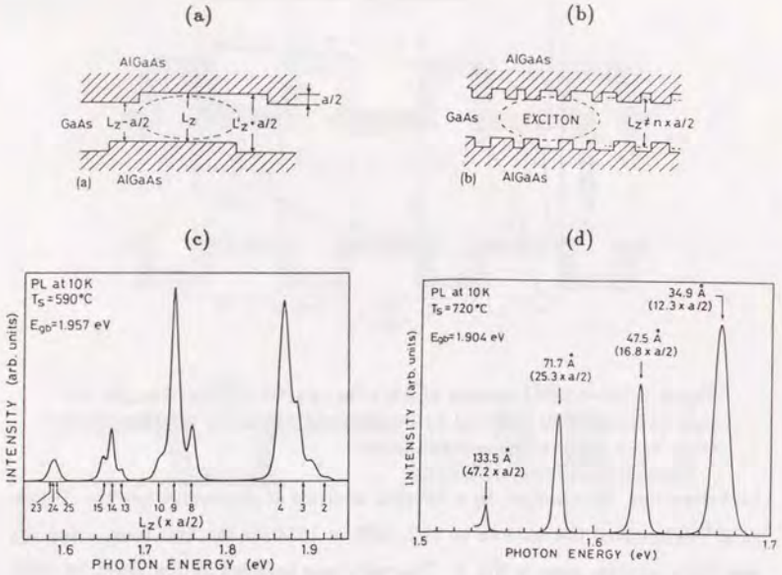

Figure 3 (a) and (b) Schematic illustration of the interface roughness in a quantum well. (a) Model for a sample grown at low temperature with growth interruption. (b) Model for a sample grown at high temperature without growth interruption. (c) Photoluminescence spectra of a sample with four quantum wells with different thickness grown at 590°C with 2-min growth interruption. (d) Photoluminescence spectra of a similar sample but grown at 720°C without growth interruption.[6]

There are four series of peaks each of which corresponds to one of the four quantum wells. In the case of Fig. 3(c), the spectrum of each quantum well has several peaks corresponding to the variation of the well thickness by integral multiple of one monolayer thickness, $a/2$, where a is the lattice constant. On the other hand, the spectrum from each quantum well of Fig. 3(d) has a single broad peak. The sample of Fig. 3(c) was grown at 590°C and the growth was interrupted at each interface for 2 min, long enough for surface diffusion of atoms, and that of Fig. 3(d) was grown at 720°C without any growth interruption. Because of the growth interruption and the low temperature growth, the lateral size of growth islands of

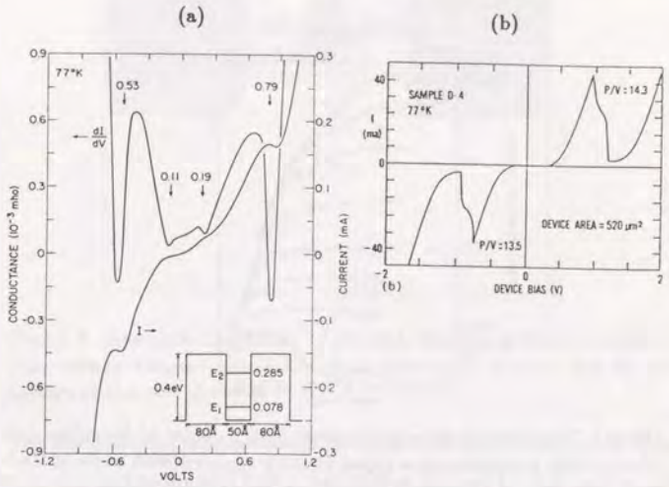

Figure 4 (a) Current and voltage characteristics of resonant tunneling observed in an $Al_{0.3}Ga_{0.7}As(80Å)/GaAs(50Å)/Al_{0.3}Ga_{0.7}As(80Å)$ double-barrier structure for the first time by Chang *et al.*,[8] (b) in an $Al_{0.3}Ga_{0.7}As/GaAs/Al_{0.3}Ga_{0.7}As$ double-barrier structure observed more recently by Huang *et al.*[9]

the sample of Fig. 3(c) is expected to be larger than the exciton diameter (~150Å) as schematically illustrated in Fig. 3(a), while that of the sample of Fig. 3(d) is expected to be much smaller than the exciton diameter as illustrated in Fig. 3(b).

The resonant-tunneling effect in a double-barrier structure was observed first by Chang *et al.*[8] and later been a subject of intensive studies. Figure 4(a) shows an example of current-voltage characteristics observed by Chang *et al.*[8] and Fig. 4(b) more recent experimental results of Huang *et al.*[9] A current maximum is observed at the applied voltage where the Fermi energy of the electrode coincides with the quasi bound state in the potential well. The ratio of current at maxima and that at minima has reached 3.9 at 300K and 14.3 at 77K for an $Al_{0.3}Ga_{0.7}As/GaAs$ system[9] and 30 at 300K and 63 at 77K for an InGaAs/AlAs/InAs system.[10] Many electronic devices based on this structure were invented[11,12] and are still being

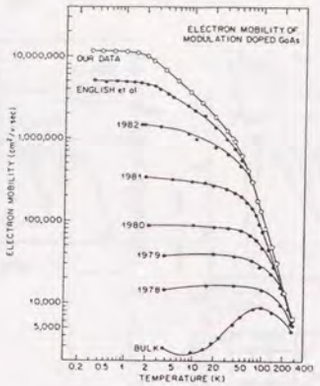

Figure 5 Temperature dependence of the Hall mobility of $Al_{0.35}Ga_{0.65}As$ /GaAs single heterostructure (open circles), together with some of landmark samples in the history of modulation-doped GaAs (closed circles).[16]

pursued. The negative differential conductivity and Bloch oscillation due to the negative mass effect, which were predicted in the original paper by Esaki and Tsu,[1] have not been observed. All experimental data of negative differential conductivity in superlattices have been interpreted by a microscopic high-field-domain formation. Quite recently Sibille *et al.*[13] observed a reduction of differential conductivity due to the negative mass effect, but could not find negative differential conductivity.

Conduction of electrons in the direction parallel to layers was studied in $GaAs/Al_xGa_{1-x}As$ superlattices by Chang *et al.*[14] for the first time in 1977. The observed electron mobility μ was merely 1200 $cm^2V^{-1}s^{-1}$, which is even smaller than that of bulk GaAs. In the next year, Dingle *et al.*[15] proposed the modulation-doped structure, in which only $Al_xGa_{1-x}As$ barrier layers are doped and carriers are introduced in GaAs potential wells spatially separated from the ionized impurities. Owing to the modulation doping and more importantly the progress of crystal growth techniques, the low-temperature mobility was improved considerably. Recently, Pfeiffer *et al.*[16] succeeded in achieving the highest mobility observed so far in a $GaAs/Al_{0.35}Ga_{0.65}As$ single heterostructure. As shown in Fig. 5, the observed mobility exceeds 10^7 $cm^2V^{-1}s^{-2}$ below 2 K.

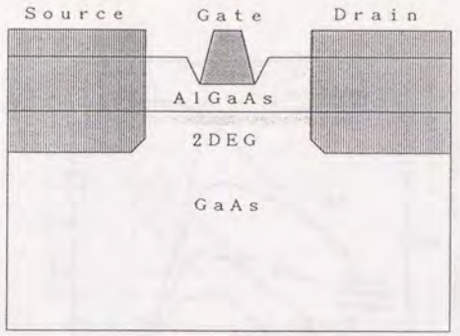

Figure 6 Schematic illustration of the high-electron-mobility transistor. The current between source and drain electrodes is controlled by the voltage of the gate electrode.

The high-mobility two-dimensional electron system attracted much attention. From the viewpoint of pure physics, this system is ideal for the study of various phenomena which are easily disturbed by impurity scattering and usually unobservable in other systems. The fractional quantum Hall effect was for example observed in this system for the first time.[17]

In device application, the electron mobility is one of the most important factors that determine the performance of electron devices. For example, the speed of logic circuits constructed by field-effect transistors is determined by the charging and discharging time of the gate electrodes. These times are nothing but the traversal time of carriers in each transistor, *i.e.*, the size of the transistor divided by the effective carrier velocity. Because the carrier velocity is usually proportional to the effective mobility, the high mobility in modulation-doped structures is certainly an attractive feature.

In 1980, Mimura *et al.*[18] invented the high-electron-mobility transistor shown schematically in Fig. 6. Electrons are located close to the $GaAs/Al_xGa_{1-x}As$ interface in the GaAs layer, separated from the donors in the $Al_xGa_{1-x}As$ layer. This high-performance device is now being used for amplifiers in parabolic antennas of the satellite television system. Integrated circuits with this device are being pursued.

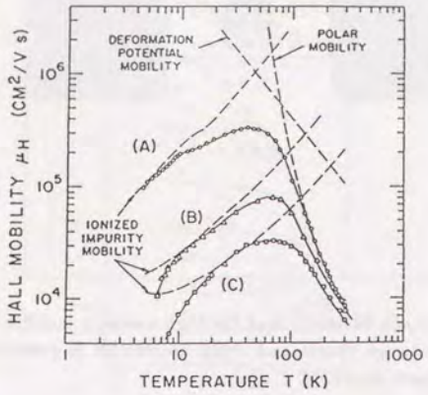

Figure 7 Temperature dependence of the Hall mobility (for magnetic field 5kG) for three n-type bulk GaAs samples with donor densities 5×10^{13}cm^{-3} (A), 10^{15}cm^{-3} (B), and 5×10^{15}cm^{-3} (C).[19] The open circles represent experimental results and dashed lines calculated results separated into contributions of different processes.

Owing to extensive theoretical and experimental studies the low-temperature mobility in heterostructures parallel to the layers is now well understood. However, usual devices function around room temperature. Figure 7 gives the temperature dependence of electron mobility in bulk GaAs, which shows clearly that the polar–optical-phonon scattering is dominant in determining the mobility above liquid-nitrogen temperature. Therefore, it is necessary and desirable to understand the electron–optical-phonon interaction in heterostructures. At early stages, many calculations were performed within a bulk-phonon model in which the usual Fröhlich interaction with *bulk* LO phonons of the material of the well layer is assumed.[20–23]

It is known that optical phonons are strongly modified by the presence of interfaces. The simplest model that can demonstrate this fact is the so-called dielectric continuum model,[24–28] in which each layer is replaced by a dielectric medium having a frequency-dependent dielectric constant. This model gives two kinds of modes, *confined* modes and *interface* modes. The confined modes have amplitudes only in one kind of layers and frequencies of either bulk LO or TO

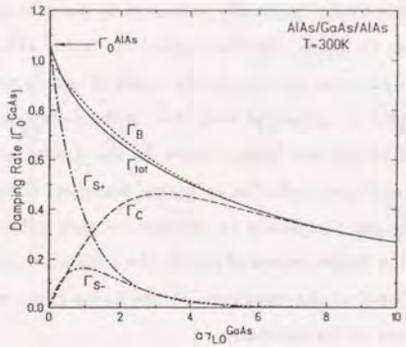

Figure 8 Damping rate, *i.e.*, (scattering rate)$\times\hbar/2$, of polarons in an AlAs/GaAs/AlAs quantum well at 300K calculated in the dielectric continuum model.[30] Γ_C is the contribution of confined modes, Γ_{S+} and Γ_{S-} are those of two kinds of interface modes, and $\Gamma_{\rm tot}$ is the total damping rate, *i.e.*, $\Gamma_{\rm tot}=\Gamma_C+\Gamma_{S+}+\Gamma_{S-}$. Γ_B is the result calculated in bulk-phonon model. $\gamma_{\rm LO}^{\rm GaAs}$ is the change of wave vector for the LO phonon of GaAs which is almost independent of a.

phonons. The interface modes, sometimes called the Fuchs-Kliewer modes,[29] have frequencies strongly dependent on the wave vector direction and amplitudes in both kinds of layers decaying exponentially away from interfaces.

Various aspects of the electron-phonon interactions have been investigated in the dielectric continuum model. For example, Mori and Ando[30] calculated the polaron scattering rate and magneto-phonon-resonance spectra for a GaAs/AlAs single heterostructure and quantum well. Their result for the polaron scattering rate in a single quantum well is shown in Fig. 8. They found that the contribution of the confined modes decreases and that of the interface modes increases with decreasing layer thickness. The total scattering rate turned out to be very similar to that of the bulk-phonon model.[22] They showed that this is closely related to a sum rule existing among the form factors for the electron-phonon matrix element.

Phonons in superlattices have been observed directly in Raman-scattering experiments and results have been analyzed based on a linear-chain model. In spite

of the simplicity, this model is usually sufficient in describing modes with wave vector perpendicular to layers. It was applied to GaAs/AlAs superlattices and showed that optical phonons are completely confined within either GaAs or AlAs layers.[31-40] This result is consistent with that of the dielectric continuum model, since only confined modes are present even in the dielectric continuum model when the wave vector is perpendicular to layers. However, if we look at the results more carefully, they are completely in contrast to each other. In the dielectric continuum model, the displacement of ions in the z direction perpendicular to the layers becomes extremal at the interfaces. In the linear-chain model, however, the displacement vanishes at the interfaces.

This disagreement between the result of the dielectric continuum model and the linear-chain model has led to a strong doubt on the validity of the former model and proposals of various new phonon models. Sawaki[41] calculated the scattering rate in GaAs/AlAs superlattices, assuming that electrons interact only with LO phonons confined to the same layer, *i.e.*, those having nodes at the interfaces. The results showed that the scattering rate decreases with narrowing of the well layer in contrast to the result in the dielectric continuum model. Ridley[42] imposed an artificial boundary condition on the confined modes of the dielectric continuum model that the z component of the displacement and the z derivative of the parallel components should vanish at the interfaces based on the result of Babiker.[43]. The resulting scattering rate increases almost linearly with increasing layer thickness but its absolute value is much smaller than that obtained in the dielectric continuum model. Huang and Zhu[44] proposed another boundary condition that both value and z derivative of the potential associated with lattice displacement should vanish at interfaces. This leads to vanishing displacement at the interfaces in agreement with the linear-chain model. This model was used also for the calculation of the scattering rate and gave another different answer.[45] Figure 9 illustrates schematically the displacements of a typical phonon with longest wavelength in these different models.

The purpose of this thesis is to resolve such confusions and controversies and clarify the electron–optical-phonon interaction in semiconductor superlattices. We

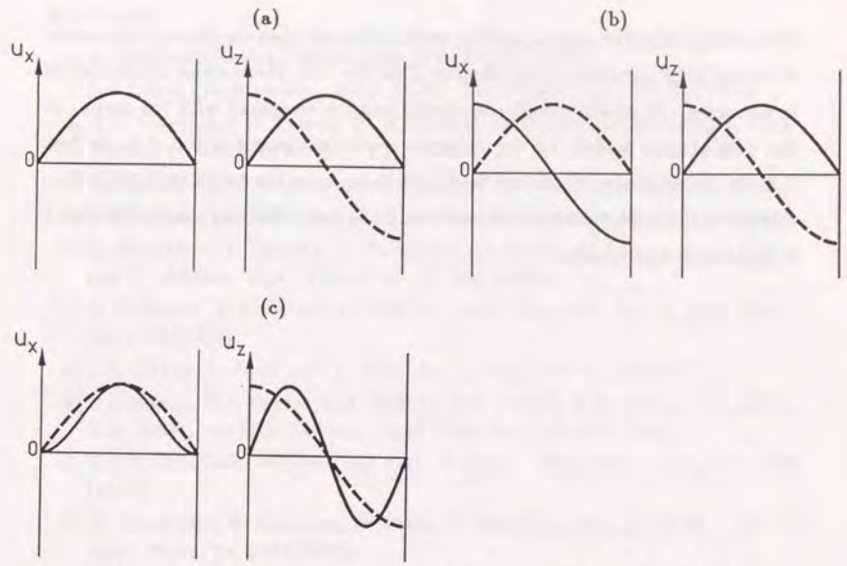

Figure 9 Schematic illustrations of displacements of confined phonon modes with longest wavelength in models proposed by (a) Sawaki,[41] (b) Ridley,[42] and (c) Huang and Zhu.[44] Dashed lines represent the result in the dielectric continuum model. The abscissa shows the z direction.

proceed as follows: Firstly, we perform a lattice-dynamical calculation of phonons in GaAs/AlAs systems and clarify their essential features. Secondly, we develop a continuum approximation which reproduces the results of this calculation for long-wavelength optical phonons dominating the electron-phonon interaction. Finally, we calculate the electron-phonon scattering rate using this model and compare the results with those obtained in different models.

The organization is as follows: In Sec. 2-1, a brief review of the simple models for phonons is given. A lattice-dynamical method for calculating phonon spectra is presented in Sec. 2-2. Calculated results for GaAs/AlAs superlattices are presented in Sec. 2-3. We develop an envelope-function approximation which reproduces the results obtained by the lattice-dynamical calculation quite well in Sec. 2-4. The results on GaSb/AlSb and GaP/AlP superlattices are presented in Sec. 2-5. Using

the envelope-function approximation, we calculate the electron-phonon interaction in GaAs/AlAs superlattices in Chapter 3. In Sec. 3-1, the method of calculation is presented. Numerical results are shown and are compared with the results in the bulk-phonon model and the dielectric continuum model in Sec. 3-2. In Sec. 3-3, the completeness of phonon modes is shown to be the origin of the fact that scattering rates calculated in different models do not differ very much. Chapter 4 is devoted to a summary.

References

1. L. Esaki and R. Tsu, IBM J. Res. Dev. **14**, 61 (1970).
2. L.L Chang, A. Segmüller, and L.Esaki, Appl. Phys. Lett. **28**, 39 (1976).
3. A.C. Gossard, P.M. Petroff, W. Wiegmann, R. Dingle, and A. Savage, Appl. Phys. Lett. **29**, 323 (1976).
4. R. Dingle, W. Wiegmann, and C. Henry, Phys. Rev. Lett. **33**, 827 (1974).
5. R.C. Miller, D.A. Kleinman, and A.C. Gossard, Phys. Rev. B **29**, 7085 (1984).
6. T. Hayakawa, T. Suyama, K. Takahashi, M. Kondo, S. Yamamoto, S. Yano, and T. Hijikata, Appl. Phys. Lett. **47**, 952 (1985).
7. L. Goldstein, Y. Horikoshi, S. Tarucha, and H. Okamoto, Jpn. J. Appl. Phys., **22**, 1489 (1983).
8. L.L. Chang, L. Esaki, and R. Tsu, Appl. Phys. Lett. **24**, 593 (1974).
9. C.I. Huang, M.J. Paulus, C.A. Bozada, S.C. Dudley, K.R. Evans, C.E. Stutz, R.L. Jones, and M.E. Cheney, Appl. Phys. Lett. **51**, 121 (1987).
10. T.P.E. Broekaert, W. Lee, and C.G. Fonstad, Appl. Phys. Lett. **53**, 1545 (1988).
11. N. Yokoyama, K. Imamura, S. Muto, S. Hiyamizu, and H. Nishi, Jpn. J. Appl. Phys. **24**, L853 (1985).
12. F. Capasso, R.A. Kiehl, J. Appl. Phys. **58**, 1366 (1985).
13. A. Sibille, J.F. Palmier, H. Wang, and F. Mollot, Phys. Rev. Lett. **64**, 52 (1990).
14. L.L. Chang, H. Sakaki, C.A. Chang, and L. Esaki, Phys. Rev. Lett. **38**, 1489 (1977).
15. R. Dingle, H.L. Störmer, A.C. Gossard, and W. Wiegmann, Appl. Phys. Lett. **33**, 665 (1978).
16. L. Pfeiffer, K.W. West, H.L. Stormer, and K.W. Baldwin, Appl. Phys. Lett. **55**, 1888 (1989).
17. D.C. Tsui, H.L. Stormer, and A.C. Gossard, Phys. Rev. Lett. **48**, 1559 (1982).
18. T. Mimura, S. Hiyamizu, T. Fujii, and K. Nanbu, Jpn. J. Appl. Phys. **19**, L225 (1980).
19. G.E. Stillman, C.M. Wolfe, and J.O. Dimmock, J. Phys. Chem. Solids **31**, 1199 (1970).
20. D.K. Ferry, Surf. Sci. **75**, 86 (1978).
21. K. Hess, Appl. Phys. Lett. **35**, 484 (1979).
22. P.J. Price, Ann. Phys. **133**, 217 (1981); Phys. Rev. B **30**, 2234 (1984).
23. S. Das Sarma and B.A. Mason, Ann. Phys. **163**, 78 (1985).

24. S.M. Rytov, Sov. Phys. JETP **2**, 466 (1956).
25. E.P. Pokatilov and S.I. Beril, Phys. Status Solidi B **110**, K75 (1982); **118**, 567 (1983).
26. R.E. Camley and D.L. Mills, Phys. Rev. B **29**, 1695 (1984).
27. R. Lassnig, Phys. Rev. B **30**, 7132 (1984).
28. M. Nakayama, M. Ishida, and N. Sano, Phys. Rev. B **38**, 6348 (1988).
29. R. Fuchs and K.L. Kliewer, Phys. Rev. **140**, A2076 (1965).
30. N. Mori and T. Ando, Phys. Rev. B **40**, 6175 (1989).
31. R. Tsu and S.S. Jha, Appl. Phys. Lett. **20**, 16 (1972).
32. J.L. Merz, A.S. Barker, Jr., and A.C. Gossard, Appl. Phys. Lett. **31**, 117 (1977).
33. A.S. Barker, Jr., J.L. Merz, and A.C. Gossard, Phys. Rev. B **17**, 3181 (1978).
34. N. Sawaki and N. Akasaki, Physica **134B**, 494 (1985).
35. C. Colvard, T.A. Gant, M.V. Klein, R. Merlin, R. Fischer, H. Morkoç, and A.C. Gossard, Phys. Rev. B **31**, 2080 (1985).
36. B. Jusserand, D. Paquet, A. Regreny, and J. Kervarec, J. Phys. (Paris) Colloq. **45**, C5-145 (1984).
37. M. Nakayama, K. Kubota, H. Kato, S. Chika, and N. Sano, Solid State Commun. **53**, 493 (1985).
38. M. Nakayama, K. Kubota, K. Kanata, H. Kato, S. Chika, and N. Sano, Jpn. J. Appl. Phys. **24**, 1331 (1985).
39. A. Fasolino, E. Molinari, and J.C. Maan, Phys. Rev. B **33**, 8889 (1986).
40. B. Zhu and K.A. Chao, Phys. Rev. B **36**, 4906 (1987).
41. N. Sawaki, J. Phys. C **19**, 4965 (1986).
42. B.K. Ridley, Phys. Rev. B **39**, 5282 (1989).
43. M. Babiker, J. Phys. C **19**, 683 (1986).
44. K. Huang and B.F. Zhu, Phys. Rev. B **38**, 2183 (1988) ; Phys. Rev. B **38**, 13377 (1988).
45. S. Rudin and T.L. Reinecke, Phys. Rev. B **41**, 7713 (1990).

Chapter 2

Phonons in Superlattices

2-1 Simple Models

2-1-1 Linear-Chain Model

One simple model for phonons in semiconductor superlattices is a linear-chain model with only nearest-neighbor interaction.[1-9] This model is explained in many elementary textbooks of solid-state physics.[10] For longitudinal phonons with wave vector along the [100] direction in crystals having the zinc-blende structure, each atomic layer perpendicular to the wave vector moves rigidly. Therefore, we can replace each atomic layer by one atom as shown in Fig. 1. The same is applicable to transverse modes with displacements in the [110] or [1$\bar{1}$0] direction. A unit cell contains two atoms, which satisfy the following equations of motion

$$\begin{aligned} M_c \frac{d^2 u_c(s)}{dt^2} &= f_2[-u_c(s) + u_a(s-1)] + f_1[-u_c(s) + u_a(s)], \\ M_a \frac{d^2 u_a(s)}{dt^2} &= f_1[-u_a(s) + u_c(s)] + f_2[-u_a(s) + u_c(s+1)], \end{aligned} \tag{2.1}$$

where M_i and u_i are the mass and the displacement, respectively, of atom i $(=c, a)$, c and a denoting cation (positive ion) and anion (negative ion), respectively, f_1 and f_2 are force constants, and s is the coordinate denoting cell number. We have $f_1 = f_2$ for longitudinal modes and $f_1 \neq f_2$ for transverse modes. Usually $f_1 \gg f_2$

or $f_1 \ll f_2$ because of the nature of the tetrahedral bond structure (see Fig. 16 of Sec. 2-3-3, for example). Substituting the solution of traveling wave

$$\begin{aligned} u_c(s) &= \frac{U_1}{\sqrt{M_c}} \exp[i(q\frac{a}{2}s - \omega t)], \\ u_a(s) &= \frac{U_2}{\sqrt{M_a}} \exp[i(q\frac{a}{2}s - \omega t)], \end{aligned} \tag{2.2}$$

in Eq. (2.1), we obtain

$$\begin{aligned} \omega^2 U_1 &= \frac{f_1 + f_2}{M_c} U_1 - \frac{f_1 + f_2 e^{-iqa/2}}{\sqrt{M_c M_a}} U_2, \\ \omega^2 U_2 &= -\frac{f_1 + f_2 e^{iqa/2}}{\sqrt{M_c M_a}} U_1 + \frac{f_1 + f_2}{M_a} U_2, \end{aligned} \tag{2.3}$$

where a is the lattice constant, q is the wave vector, ω is the angular frequency, and $U_i = \sqrt{M_i} u_i$ is reduced displacement of atom i. Diagonalizing the *dynamical matriz* which is the coefficient of U_1 and U_2, we obtain

$$\omega^4 - \frac{M_c + M_a}{M_c M_a}(f_1 + f_2)\omega^2 + \frac{2 f_1 f_2}{M_c M_a}[1 - \cos(q\frac{a}{2})] = 0, \tag{2.4}$$

and

$$\frac{U_2}{U_1} = \frac{\frac{1}{\sqrt{M_c M_a}}(f_1 + f_2 e^{iqa/2})}{\frac{f_1 + f_2}{M_a} - \omega^2}. \tag{2.5}$$

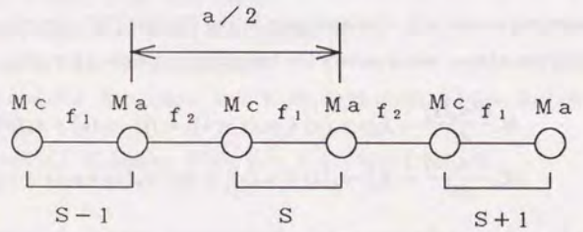

Figure 1 A schematic illustration for bulk material with two atoms in a unit cell.

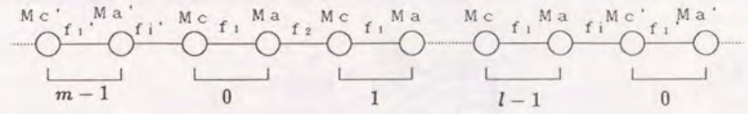

Figure 2 A schematic illustration for a superlattice with l atomic layers of material 1 and m atomic layers of material 2.

Turning now to the case of the superlattice shown in Fig. 2, the conventional method of lattice dynamics requires diagonalization of a $2n \times 2n$ dynamical matrix with $n = l + m$. This model with $f_1 = f_2$ was applied to GaAs/AlAs superlattices for the first time by Tsu and Jha[1] for calculations of phonon and polariton modes in 1972. They found that there are many optical modes in superlattices. Merz *et al.*[2] and Barker *et al.*[3] used it for analysis of Raman spectra and pointed out that f_1 and f_2 should be different for TO modes. Figure 3 shows atomic displacements calculated in this model by Sawaki and Akasaki.[4] They claimed that the envelope of the displacement can be described by sinusoidal curves having nodes at a plane in the vicinity of the interfaces. In general, this model gives the following results. In the frequency region where the bulk frequency of modes with the same symmetry of two constituents overlap each other, phonon modes exhibit dispersion and the displacements extend through the whole crystal. On the other hand, in the frequency region where the bulk frequencies do not overlap, phonon modes are confined to either layer, exhibit no dispersion, and the displacements drop to zero at the interfaces. Similar results will be obtained in the lattice-dynamical calculation in Sec. 2-3. Note that this model is not applicable when the wave vector is not perpendicular to the layers.

For superlattices with long period, the direct numerical diagonalization of the dynamical matrix is quite time consuming. Jusserand *et al.*[6] proposed a convenient method in which solutions of bulk phonons are matched at the interfaces and the problem is reduced to an eigenvalue problem of 4×4 matrix. See Appendix A for more details.

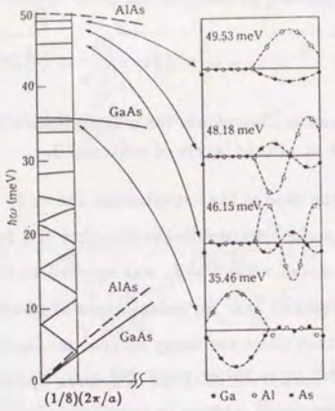

Figure 3 Dispersion relation and displacement of ions of some LO modes in a $(GaAs)_4(AlAs)_4$ superlattice calculated in the linear-chain model.[4]

2-1-2 Elastic Continuum Model[11-14]

If each layer is much thicker and the wave length is much larger than the lattice constant, we can use an elastic continuum model for acoustic modes. An elastic wave propagating along the z axis is then subject to the equation

$$\rho(z)\frac{\partial^2 u(z)}{\partial t^2} = \frac{\partial}{\partial z}\Big[C(z)\frac{\partial u(z)}{\partial z}\Big], \tag{2.6}$$

where $\rho(z)$ is a mass density, $C(z)$ is an elastic constant, and $u(z)$ is an atomic displacement at z. More explicitly

$$\rho_l\frac{\partial^2 u_l}{\partial t^2} = C_l\frac{\partial^2 u_l}{\partial z^2}, \qquad (l=1,2), \tag{2.7}$$

which has a solution

$$u_l(z) = A_l e^{i\left[q_l(\omega)z-\omega t\right]} + B_l e^{-i\left[q_l(\omega)z-\omega t\right]}. \tag{2.8}$$

Substituting this solution into Eq. (2.7), we obtain

$$\frac{\omega}{q_l(\omega)} = \sqrt{\frac{C_l}{\rho_l}} = v_l. \tag{2.9}$$

We impose two boundary conditions at each of two interfaces: the continuity of the displacement

$$u_1(z) = u_2(z), \tag{2.10}$$

and the continuity of the stress

$$C_1\frac{\partial u_1}{\partial z} = C_2\frac{\partial u_2}{\partial z}. \tag{2.11}$$

These conditions give a 4×4 secular equation, which leads to the dispersion relation

$$\cos(qd) = \cos\Big[\omega\Big(\frac{d_1}{v_1}+\frac{d_2}{v_2}\Big)\Big] - \frac{\epsilon^2}{2}\sin\Big(\frac{\omega d_1}{v_1}\Big)\sin\Big(\frac{\omega d_2}{v_2}\Big), \tag{2.12}$$

with

$$\epsilon = \frac{\rho_2 v_2 - \rho_1 v_1}{(\rho_2 v_2 \rho_1 v_1)^{1/2}}, \tag{2.13}$$

where q is the wave vector, d_1 and d_2 are the thickness of the layer 1 and 2, respectively, and $d = d_1 + d_2$ is the superlattice period. This dispersion is similar to that of the Kronig-Penney model for electrons. Because ϵ is usually small ($\epsilon^2/2 \sim 10^{-2}$ for GaAs/AlAs), the second term in the right hand side of Eq. (2.12) can be neglected and we obtain

$$q(d_1+d_2) = \pm\omega\Big(\frac{d_1}{v_1}+\frac{d_2}{v_2}\Big) + 2\pi\nu, \qquad \nu = 0,\ \pm1,\ \pm2\ldots \tag{2.14}$$

which corresponds to an average of the elastic dispersions of two materials folded at new Brillouin zone boundaries. The sound velocity is given by the following average

$$v = \frac{v_1 v_2(d_1+d_2)}{d_1 v_2 + d_2 v_1}. \tag{2.15}$$

If we take into account nonvanishing ϵ, small gaps open up at the center and the edges of the folded Brillouin zone. This result will be confirmed by the lattice-dynamical calculation in Sec. 2-3.

2-1-3 Dielectric Continuum Model

In the frequency region of optical phonons, we can adopt another continuum model called "a dielectric continuum model."[15-19] This model can be used only in the long wavelength limit, where the dispersion of optical modes can be ignored completely.

We write the displacement of cations and anions as $\mathbf{u}_c(\mathbf{r},t)$ and $\mathbf{u}_a(\mathbf{r},t)$, respectively. The equations of motion are given by

$$M_c\ddot{\mathbf{u}}_c(\mathbf{r},t) = -f\,[\mathbf{u}_c(\mathbf{r},t) - \mathbf{u}_a(\mathbf{r},t)] + Ze\mathbf{E}(\mathbf{r},t), \tag{2.16}$$

$$M_a\ddot{\mathbf{u}}_c(\mathbf{r},t) = f\,[\mathbf{u}_c(\mathbf{r},t) - \mathbf{u}_a(\mathbf{r},t)] - Ze\mathbf{E}(\mathbf{r},t), \tag{2.17}$$

where M_c and M_a are the mass of cations and anions, respectively, f is the force constant, Ze is the effective charge, and $\mathbf{E}$ is the electric field. With the reduced mass $M = M_cM_a/(M_c+M_a)$ and the envelope of the relative displacement $\mathbf{u} = \mathbf{u}_c - \mathbf{u}_a$, we obtain

$$-\omega^2 M\mathbf{u}(\mathbf{r},t) = -M\omega_{\mathrm{TO}}^2\mathbf{u}(\mathbf{r},t) + Ze\mathbf{E}(\mathbf{r},t), \tag{2.18}$$

where $\omega_{\mathrm{TO}} = \sqrt{f/M}$ is the TO phonon frequency. The displacement of anions and cations are determined by $\mathbf{u}_c = M_a\mathbf{u}/(M_a+M_c)$ and $\mathbf{u}_c = -M_c\mathbf{u}/(M_a+M_c)$, respectively.

The polarization $\mathbf{P}$ is determined by

$$\mathbf{P} = nZe\mathbf{u} + \alpha_i\mathbf{E}, \tag{2.19}$$

where the second term represents the effect of the deformation of ions, α_i is a appropriate coefficient, and n is the number of cation-anion pairs in a unit volume,

i.e., $n = 4/a^3$ for zinc-blende crystals. Combining Eqs. (2.18) and this equation, we obtain

$$\mathbf{P} = \Big(\frac{(Ze)^2 n}{M(\omega_{\mathrm{TO}}^2 - \omega^2)} + \alpha_i\Big)\mathbf{E}. \tag{2.20}$$

The electric displacement $\mathbf{D}$ becomes

$$\mathbf{D} = \mathbf{E} + 4\pi\mathbf{P} = \epsilon(\omega)\mathbf{E} \tag{2.21}$$

where $\epsilon(\omega)$ is the dielectric constant at frequency ω, given by

$$\epsilon(\omega) = \epsilon_\infty\frac{\omega_{\mathrm{LO}}^2 - \omega^2}{\omega_{\mathrm{TO}}^2 - \omega^2}, \tag{2.22}$$

with ϵ_∞ the high frequency dielectric constant and ω_{LO} the LO phonon frequency. We have

$$\alpha_i = \frac{\epsilon_\infty - 1}{4\pi}, \tag{2.23}$$

and

$$Ze = \sqrt{\frac{M}{n}}\epsilon_\infty\omega_{\mathrm{LO}}\sqrt{\frac{1}{4\pi}\Big(\frac{1}{\epsilon_\infty} - \frac{1}{\epsilon_0}\Big)}, \tag{2.24}$$

with ϵ_0 the static dielectric constant. The LO frequency ω_{LO} is given by the Lyddane-Sachs-Teller relation

$$\omega_{\mathrm{LO}}^2 = \frac{\epsilon_0}{\epsilon_\infty}\omega_{\mathrm{TO}}^2, \tag{2.25}$$

and the displacement is related to the electric field through

$$\mathbf{u} = \frac{1}{4\pi nZe}[\epsilon(\omega) - \epsilon_\infty]\mathbf{E}. \tag{2.26}$$

This model is equivalent to Maxwell's equations

$$\mathrm{rot}\mathbf{E} = 0, \tag{2.27}$$

$$\mathrm{div}\mathbf{D} = 0. \tag{2.28}$$

In terms of the electrostatic potential Φ, defined by

$$\mathbf{E} = -\nabla \Phi, \tag{2.29}$$

we obtain

$$\epsilon(\omega) \triangle \Phi(\mathbf{r}) = 0. \tag{2.30}$$

In superlattices, Φ can be expanded as

$$\Phi(\mathbf{r}) = \sum_{q_\parallel} \Phi_{q_\parallel}(z) e^{i(q_\parallel r_\parallel - \omega t)}, \tag{2.31}$$

where $q_\parallel$ is the component of wave vector parallel to the layers. Substitution of Eq. (2.31) into Eq. (2.30) yields

$$\epsilon(\omega)\Big[\frac{d^2\Phi_{q_\parallel}(z)}{dz^2} - q_\parallel^2 \Phi_{q_\parallel}(z)\Big] = 0. \tag{2.32}$$

This equation is satisfied for

$$\epsilon(\omega) = 0 \tag{2.33}$$

or

$$\frac{d^2\Phi_{q_\parallel}(z)}{dz^2} - q_\parallel^2 \Phi_{q_\parallel}(z) = 0. \tag{2.34}$$

For solutions satisfying Eq. (2.33) in layer 1, for example, we obtain $\omega = \omega_{\rm LO}$ from Eq. (2.22). In general, the LO phonon frequencies in layers 1 and 2 are different. Then, in layer 2, the potential must satisfy Eq. (2.34). The continuity of z component of $\mathbf{D}$ requires that the z derivative of Φ vanishes at the interfaces, leading to $\Phi = 0$ in layer 2. Moreover, the continuity of the potential at the interfaces requires that the potential inside layer 1 vanishes at the interfaces. We choose the coordinate system in such a way that one layer of $l=1$ occupies region $0<z<d_1$ and that of $l=2$ occupies region $-d_2<z<0$. Then, the potential $\Phi_{q_\parallel}$ in these layers can be written as

$$\Phi_{q_\parallel}(z) \propto \sin\Big(\frac{m\pi}{d_l}(z - z_{C,l})\Big) \quad m = 1, 2, 3 \ldots, \tag{2.35}$$

where $z_{C,1}=0$ and $z_{C,2}=-d_2$. For simplicity, we assume that $q_\parallel$ is in the xz plane. The displacement can be obtained from Eq. (2.26) as

$$\mathbf{u}(z) = \Big(iq_\parallel \sin\Big(\frac{m\pi}{d_l}(z - z_{C,l})\Big), 0, -\frac{m\pi}{d_l}\cos\Big(\frac{m\pi}{d_l}(z - z_{C,l})\Big)\Big)u, \tag{2.36}$$

where u is a normalization coefficient. These modes are infinitely degenerate, since their frequency is independent of m. There are also infinitely degenerate transverse modes with frequency $\omega_{\rm TO}$ and nonzero amplitude only in one of the layers. These modes are all called "confined modes."

Next, we consider solutions of Eq. (2.34) which are called "interface" or "Fuchs-Kliewer" modes.[20] We have

$$\Phi_{q_\parallel}(z) = C_{S,l}\cosh[q_\parallel(z - z_{I,l})] + C_{A,l}\sinh[q_\parallel(z - z_{I,l})] \tag{2.37}$$

in each layer, where $z_{I,1} = d_1/2$, $z_{I,2} = -d_2/2$, C's are coefficients to be determined, and subscripts A and S denote symmetric and antisymmetric components, respectively. The boundary conditions of continuity of the parallel component of $\mathbf{E}$ and the perpendicular component of $\mathbf{D}$ can be written as

$$\begin{aligned}
&C_{S,1}\cosh\Big(\frac{q_\parallel d_1}{2}\Big) + C_{A,1}\sinh\Big(\frac{q_\parallel d_1}{2}\Big) \\
&\qquad = C_{S,2}\cosh\Big(-\frac{q_\parallel d_2}{2}\Big) + C_{A,2}\sinh\Big(-\frac{q_\parallel d_2}{2}\Big), \\
&\Big[C_{S,1}\cosh\Big(-\frac{q_\parallel d_1}{2}\Big) + C_{A,1}\sinh\Big(-\frac{q_\parallel d_1}{2}\Big)\Big]e^{iq_x d} \\
&\qquad = C_{S,2}\cosh\Big(\frac{q_\parallel d_2}{2}\Big) + C_{A,2}\sinh\Big(\frac{q_\parallel d_2}{2}\Big), \\
&\epsilon_1(\omega)\Big[C_{S,1}\sinh\Big(\frac{q_\parallel d_1}{2}\Big) + C_{A,1}\cosh\Big(\frac{q_\parallel d_1}{2}\Big)\Big] \\
&\qquad = \epsilon_2(\omega)\Big[C_{S,2}\sinh\Big(-\frac{q_\parallel d_2}{2}\Big) + C_{A,2}\cosh\Big(-\frac{q_\parallel d_2}{2}\Big)\Big], \\
&\epsilon_1(\omega)\Big[C_{S,1}\sinh\Big(-\frac{q_\parallel d_1}{2}\Big) + C_{A,1}\cosh\Big(-\frac{q_\parallel d_1}{2}\Big)\Big]e^{iq_x d} \\
&\qquad = \epsilon_2(\omega)\Big[C_{S,2}\sinh\Big(\frac{q_\parallel d_2}{2}\Big) + C_{A,2}\cosh\Big(\frac{q_\parallel d_2}{2}\Big)\Big],
\end{aligned} \tag{2.38}$$

with $\epsilon_l(\omega)$ the dielectric function of bulk material l. This set of equations has a solution if and only if

$$\cos(q_z d) = \cosh(q_{\|} d_1)\cosh(q_{\|} d_2) + \frac{\epsilon_1^2(\omega)+\epsilon_2^2(\omega)}{2\epsilon_1(\omega)\epsilon_2(\omega)}\sinh(q_{\|} d_1)\sinh(q_{\|} d_2). \tag{2.39}$$

In the following, we will confine ourselves to the case that layers 1 and 2 have same thickness $d_1 = d_2 = d/2$, for simplicity. First, we should note that the frequency depends on the direction of the wave vector close to the Γ point $q_x = q_y = q_z = 0$. The anisotropy is given by the equation:

$$\frac{1}{2}\left(\frac{\epsilon_2(\omega)}{\epsilon_1(\omega)} + \frac{\epsilon_1(\omega)}{\epsilon_2(\omega)}\right) = -\left(1 + \frac{2}{\tan^2\theta}\right). \tag{2.40}$$

The displacements are independent of z within each layer and given by

$$\mathbf{u}_l = \frac{1}{4\pi n Z_l e}[\epsilon_l(\omega) - \epsilon_{\infty,l}]\begin{pmatrix} 1 \\ 0 \\ \cot\phi_l \end{pmatrix} u \qquad (l = 1, 2), \tag{2.41}$$

where u is a normalization coefficient and ϕ_1 and ϕ_2 are determined by

$$\epsilon_2 \tan\phi_1 = \epsilon_1 \tan\phi_2 = \frac{1}{2}(\epsilon_1 + \epsilon_2)\tan\theta. \tag{2.42}$$

When the wave vector parallel to the layer is nonzero, *i.e.*, $q_x \neq 0$, the displacement becomes exponentially localized, $u(z) \propto \exp(-|q_x z|)$, as a function of the distance z from the interface. In particular, for $q_z = 0$ and $q_x \neq 0$, *i.e.*, $\theta = \pi/2$, Eq. (2.39) reduces to $\epsilon_1(\omega) = -\epsilon_2(\omega)$ independent of q_x. The modes are doubly degenerate, and their frequencies are determined by setting $\theta = \pi/2$ in the above equation, *i.e.*, by the condition that $\epsilon_1(\omega) = -\epsilon_2(\omega)$ independent of q_x. The displacements are given by

$$\mathbf{u}_l = \frac{1}{4\pi n Z_l e}[\epsilon_l(\omega) - \epsilon_{\infty,l}]\exp(iq_x x)\begin{pmatrix} i\cosh q_x(z - z_{I,l}) \\ 0 \\ \sinh q_x(z - z_{I,l}) \end{pmatrix} u \tag{2.43}$$

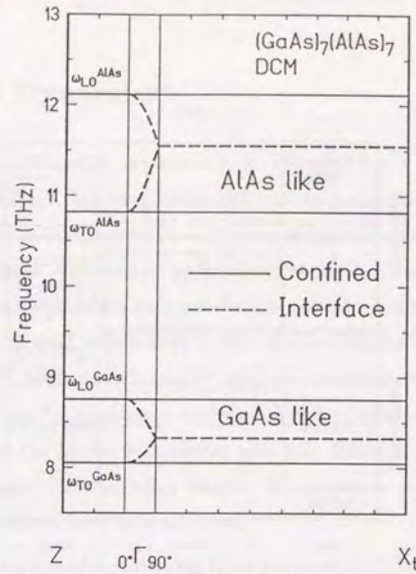

Figure 4 Phonon dispersion in a $(GaAs)_7(AlAs)_7$ superlattice calculated in the dielectric continuum model.

and

$$\mathbf{u}_l = (-1)^l \frac{1}{4\pi n Z_l e}[\epsilon_l(\omega) - \epsilon_{\infty,l}]\exp(iq_x x)\begin{pmatrix} i\sinh q_x(z - z_{I,l}) \\ 0 \\ \cosh q_x(z - z_{I,l}) \end{pmatrix} u. \tag{2.44}$$

Figure 4 shows the phonon dispersion of a $(GaAs)_7(AlAs)_7$ superlattice calculated in the dielectric continuum model. The interface modes have a frequency lying between ω_{LO} and ω_{TO} of GaAs and between ω_{LO} and ω_{TO} of AlAs. Further, they exhibit strong dependence on wave vector direction at the Γ point. There are infinitely degenerate confined modes at ω_{LO} and ω_{TO} of both GaAs and AlAs. Figure 5 shows some examples of lattice displacements of GaAs like interface modes having larger amplitude in the GaAs layer. At the Γ point, the displacement is independent of z but its relative amplitude in the GaAs and AlAs layers varies as a function of θ [see Eqs. (2.40)–(2.42)]. For a nonzero wave vector parallel to the layer, the displacement decreases exponentially away from the interfaces.

(a)

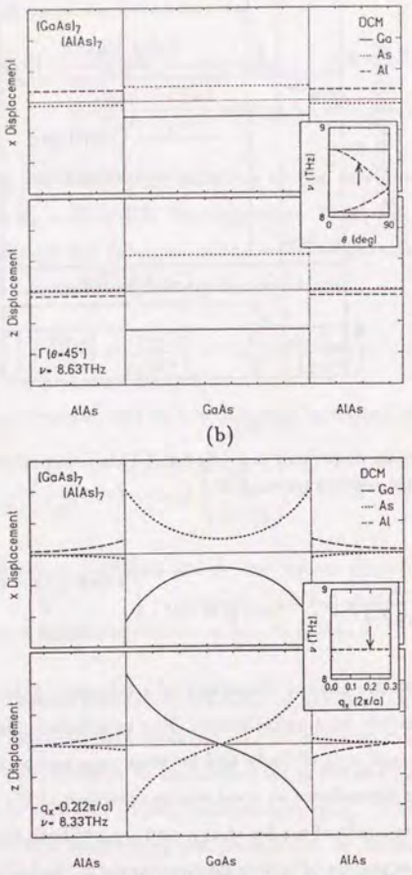

(b)

Figure 5 Displacements of ions for two interface modes in a $(GaAs)_7$ $(AlAs)_7$ superlattice (a) at the Γ point and the direction $\theta = \pi/4$ and (b) at $\mathbf{q} = (0.2\times 2\pi/a, 0, 0)$ calculated in the dielectric continuum model. The solid lines represent displacement of Ga, the dotted lines represent that of Al, and the dashed lines represent that of As. The thin vertical straight lines indicate the interface position. The inset shows a part of the dispersion curve given in Fig. 4 and the modes are indicated by the arrows. (a) and (b) should be compared with the lattice-dynamical results given in Figs. 12(a) and 14(b), respectively.

2-2 Lattice Dynamics[21]

The three models discussed in the above section give us much information about phonons in superlattices. However, their applicability is restricted and the validity of these models for real superlattices remains questionable. In the following, we investigate phonons in superlattices by lattice-dynamical calculation and develop a continuum approximation for long-wavelength optical phonons. In addition to the present work, several calculations of the phonon modes in realistic models were reported.[22–27] Richter and Strauch[24] employed a valence-overlap shell-model, Ren, Chu, and Chang[25] a rigid-ion model with eleven parameters. Chu, Ren, and Chang[26] combined the linear-chain model with the dielectric continuum model to explain the origin of the interface modes. Many review articles[28–34] on the phonons in superlattices have been appeared.

We use a rigid-ion model containing three parameters. The short-range forces are treated in the valence-force-field model, in which the potential energy for bond stretching, δE_0, and for bond bending, δE_1, is given by

$$\delta E_0 = \frac{1}{2} C_0 \left(\frac{\delta d}{d}\right)^2, \quad \text{and} \quad \delta E_1 = \frac{1}{2} C_1 (\delta\theta)^2, \tag{2.45}$$

where C_0 and C_1 are force constants, d is the equilibrium bond-length, and $\delta\theta$ the deviation from the equilibrium angle between adjacent bonds. The long-range Coulomb force is taken into account by a rigid-ion model characterized by an effective charge Ze and calculated by using the conventional Ewald method. Since ϵ_∞ of bulk III-V compound semiconductors do not differ much, we neglect the small image potentials.

The three parameters C_0, C_1, and Z are determined as follows. First, we neglect the effective charge Z. The frequency of LO and TO phonons at the Γ point is given by $\omega_0^2 = 64(C_0+8C_1)/9Ma^2$, where M is the reduced mass of cation and anion, and a is the lattice constant. This frequency is fitted to $\sqrt{\omega_{\rm LO}^2/3+2\omega_{\rm TO}^2/3}$ where $\omega_{\rm LO}$ and $\omega_{\rm TO}$ are the observed LO and TO frequencies, respectively, at the Γ point. The dispersion in the Γ–X direction or the band width of the TO phonons is determined by the ratio C_1/C_0. The observed dispersion along Γ–X direction

is well reproduced by choosing $C_1/C_0 \approx 0.025$ for both GaAs and Ge, for which reliable experimental results are available. The same ratio is chosen for AlAs because the amount of the dispersion is not well known and the short-range force constants are expected to be only weakly dependent on the constituent atoms. Strictly speaking, the phonon spectra are subject to additional modifications by the introduction of the effective charge. For example, the Coulomb interaction gives rise to a slight increase of the amount of dispersion of TO phonons along the Γ–X direction. However, such effects are small and the main role of the Coulomb interaction is to cause the splitting of LO and TO modes. The effective charge Z is thus determined easily so as to reproduce the splitting of LO and TO phonons at the Γ point. The parameters are given in Table . For the calculation in superlattices the parameters C_0, C_1, and Z at the interface are also required. The interface parameters are determined simply by an arithmetic average of the corresponding bulk values.

Figure 6 shows the phonon dispersion along Γ–X of bulk GaAs and AlAs calculated using the present parameters, together with experimental results.[35–38] The first Brillouin zone is given in Fig. 7 (a). The frequency is given in units of THz (1THz=10^{12}Hz=4.14meV). The present model reproduces all important characteristic features of the phonon modes. There remain some disagreements, especially for the frequencies at the X point of GaAs. This insufficiency is inherent to the valence-force-field model and cannot be overcome without increasing the number of parameters. In spite of this slight inadequacy the present model is certainly sufficient for the present purposes.

2-3 GaAs/AlAs Superlattices

2-3-1 Γ-Z Direction

Figure 8 shows calculated dispersion relation of a $(GaAs)_7(AlAs)_7$ superlattice. The first Brillouin zone is given in Fig. 7 (b). Let us first concentrate on the dispersion along the Γ–Z direction (the left panel). The results are essentially the same as those calculated in a simple linear-chain model with nearest-neighbor force constants, which is reasonable because the present model comes down to

	M_c (a.u.)	M_a (a.u.)	C_0 (eV)	C_1 (eV)	Z	ϵ_∞
GaAs	69.72	74.92	38.38	0.96	2.18	10.9
AlAs	26.98	74.92	38.93	0.97	2.23	8.16
GaP	69.72	30.97	39.62	0.99	2.06	8.38
AlP	26.98	30.97	39.56	0.99	2.28	7.5
GaSb	69.72	121.75	39.11	0.98	2.99	14.44
AlSb	26.98	121.75	37.84	0.95	1.86	9.88

Table I Parameters used for the present calculations. The mass of anions and cations are denoted by M_c and M_a, respectively, C_0 and C_1 are the force constant for bond-stretching and bond-bending, respectively, in units of eV, and Ze is the effective charge.

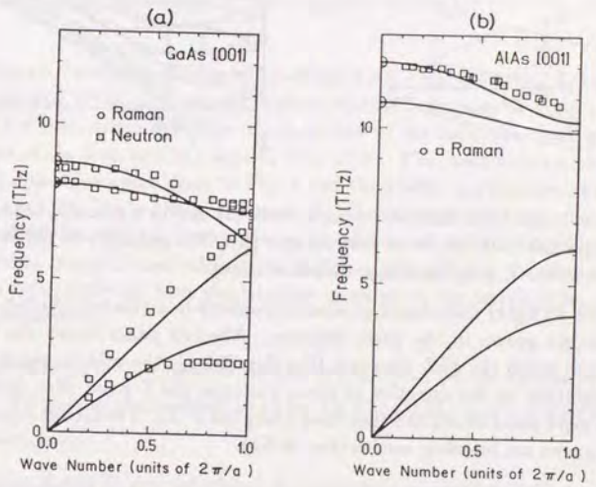

Figure 6 Dispersion relation of phonons in bulk GaAs (a) and AlAs (b) in the [001] direction calculated in the valence-force field model with three parameters C_0, C_1, and Z together with experimental results. The circles in (a) are determined by Raman scattering[35] and the squares by neutron scattering.[36] The circles and squares in (b) are both determined by Raman scattering,[37,38] but the latter in superlattices with different AlAs layer thicknesses.[38]

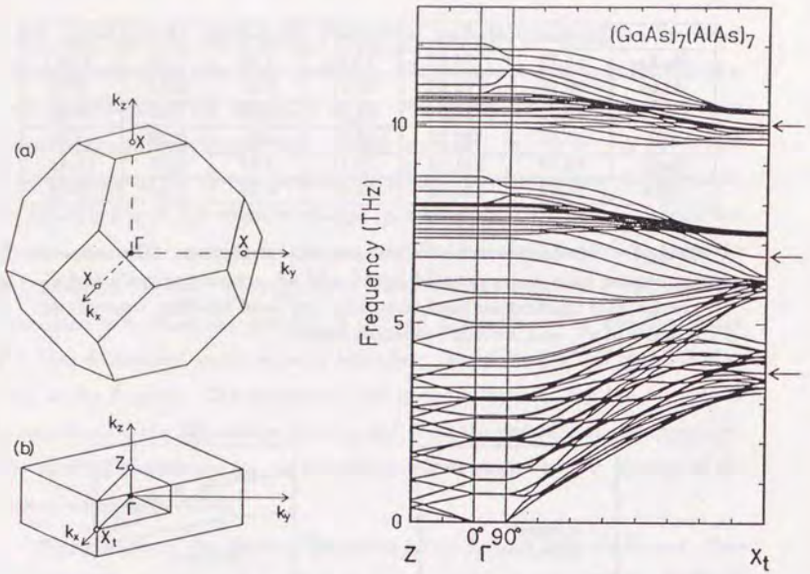

Figure 7 (left) The Brillouin zone in bulk (a) and in a $(GaAs)_n(AlAs)_m$ superlattice with $n+m$ an even integer (b). The point X_t in (b) is the same as the X point in the q_z direction in (a).

Figure 8 (right) Calculated phonon dispersions in a $(GaAs)_7(AlAs)_7$ superlattice grown in the [001] direction. The left panel shows the dispersion along the Γ–Z direction (See Sec. 2-3-1), the middle panel the dependence on the direction of the q vector at the Γ point (Sec. 2-3-2). The right panel shows the dispersion along the Γ–X_t. The modes denoted by arrows are interface modes (Sec. 2-3-3).

a linear-chain model with force constants up to next nearest-neighbor ion pairs. The long-range Coulomb interaction turns out to be not important because its force range is effectively reduced and its role is only to slightly modify nearest-neighbor and next nearest-neighbor force constants. In the region where the bulk frequencies of GaAs and AlAs overlap, acoustic modes are obtained by folding in reciprocal space and adding a very small level repulsion at mode crossings (except for modes with different symmetries), as discussed in Sec. 2-1-2. All the other

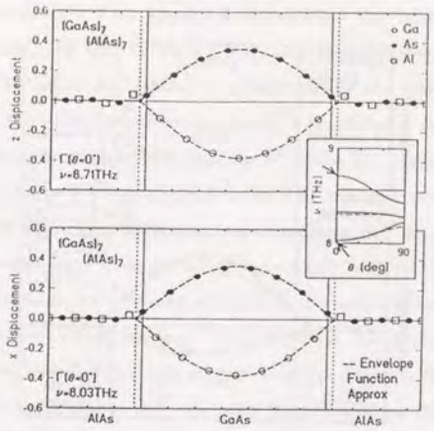

Figure 9 Calculated displacements of ions for the highest-energy LO mode (top) and TO mode (bottom) confined to the GaAs layer at the Γ point. The closed circles show the displacement of As ions, the open circles that of Ga ions, and the squares that of Al. The inset shows a part of the dispersion curve given in Fig. 8 and the modes are indicated by the arrows. The dashed lines represent the displacements calculated in the envelope-function approximation to be introduced in Sec. 2-4. The thin vertical straight lines indicate the position of interfacial As planes and the vertical dotted lines the interface position in the envelope-function approximation.

modes for which bulk frequencies do not overlap, *i.e.*, all the optical modes and some of TA modes, are confined to either GaAs or AlAs layers and exhibit only small dispersions.

Figures 9 and 10 give calculated displacements of ions for highest energy LO and TO phonons confined to the GaAs and the AlAs layer, respectively, at the Γ point (the wave vector approaches the Γ point in the z direction). The TO phonons are doubly degenerate and the figures show the modes having vanishing amplitude in the y direction at the center of the GaAs or AlAs layer. Strictly speaking, a small amplitude in the y direction in the vicinity of the interfaces does remain. The envelopes of displacement of individual ions are well approximated

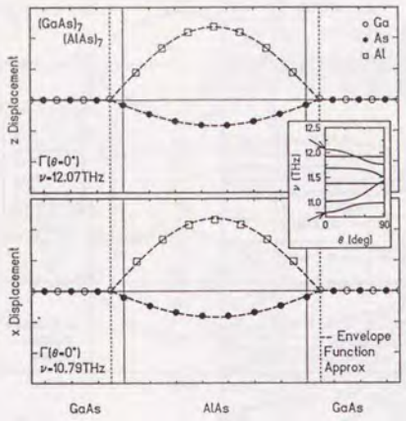

Figure 10 Calculated displacements of ions for the highest-energy LO mode (top) and TO mode (bottom) confined to the AlAs layer at the Γ point.

by sine curves with nodes between As and Al atomic planes for the GaAs-like mode and at Ga atomic planes for AlAs-like modes. Calculations for different cases reveal that in general the effective thickness for GaAs-like LO modes is $(n+0.5)\times(a/2)$ for $(GaAs)_n(AlAs)_m$ superlattices. On the other hand, in the case of AlAs-like LO phonons, the effective thickness is $(m+1)\times(a/2)$. The latter is in agreement with but the former is quite in contrast to previous suggestion[39] that the thickness is always larger by one monolayer than that of the GaAs or AlAs layer. For transverse modes, the effective thickness is larger than that for longitudinal modes, *i.e.*, $\sim(n+0.7)\times(a/2)$, $\sim(m+1.3)\times(a/2)$, for GaAs- and AlAs-like modes, respectively. Further, the thickness increases slightly for shorter wave lengths in case of GaAs-like modes. Ren *et al.*[25] have obtained a similar conclusion for GaAs-like modes but claimed that the thickness for AlAs-like modes is also given by $(m+0.5)\times(a/2)$. On the other hand, Richter *et al.*[24] have obtained the conclusion that the effective thickness is one monolayer larger for both GaAs- and AlAs-like modes in agreement with the linear-chain model. These results suggest that the effective thickness depends strongly on models.

Various experiments have already demonstrated the confinement of optical phonons in GaAs/AlAs and GaAs/$Al_xGa_{1-x}As$ superlattices.[3,5–8] There have also been some attempts to determine experimentally the effective thickness for the GaAs- and AlAs-like optical modes in $(GaAs)_n(AlAs)_m$ superlattices. Sood *et al.*[40] compared observed Raman spectra of GaAs-like optical phonons in superlattices with the bulk dispersion determined by neutron experiments. Similar experiments have been carried out also by Ishibashi *et al.*[41] In these experiments, the observed spectra have been explained reasonably well by the bulk dispersion for small wave numbers, by assuming a simple confinement effect corresponding to the effective thickness $na/2$. For large wave numbers, however, there remain significant discrepancies which strongly suggest that the effective thickness should be larger than $na/2$. Ishibashi *et al.*[41] observed Raman spectra for AlAs-like modes and demonstrated also that the effective thickness should be larger than $ma/2$. Wang *et al.*[38] determined by similar experiments the dispersion in bulk AlAs, shown in Fig. 1(b), assuming the effective thickness $(m+1)a/2$.

2-3-2 Dependence on Wave Vector Direction

As is shown in the middle panel of Fig. 8, there are essentially four modes which exhibit a strong dependence on the direction of the wave vector **q**, in terms of the angle θ, defined by $\tan\theta = q_x/q_z$ with $q=\sqrt{q_x^2+q_z^2}\to 0$. These modes lie in energy roughly between the TO and LO phonons of bulk GaAs and AlAs. The four strongly θ-dependent modes correspond to the interface modes appearing in the dielectric continuum model discussed in Sec. 2-1-3, as has already been noticed by Richter *et al.*[24]and Ren *et al.*[25]

Figure 11(a) gives the θ dependence of the optical modes with frequency close to that of the optical phonons in bulk GaAs, together with the results calculated in the dielectric continuum model. The presence of dispersion causes splittings of phonons with different number of nodes in the GaAs layer. The highest frequency mode at $\theta=0$ ($\nu=8.71$THz), which is longitudinal, has no node, and is lowered in frequency at $\theta=0$ by the confinement effect, exhibits strong θ dependence. The longitudinal mode with the second highest frequency at $\theta=0$ ($\nu=8.56$THz) with a

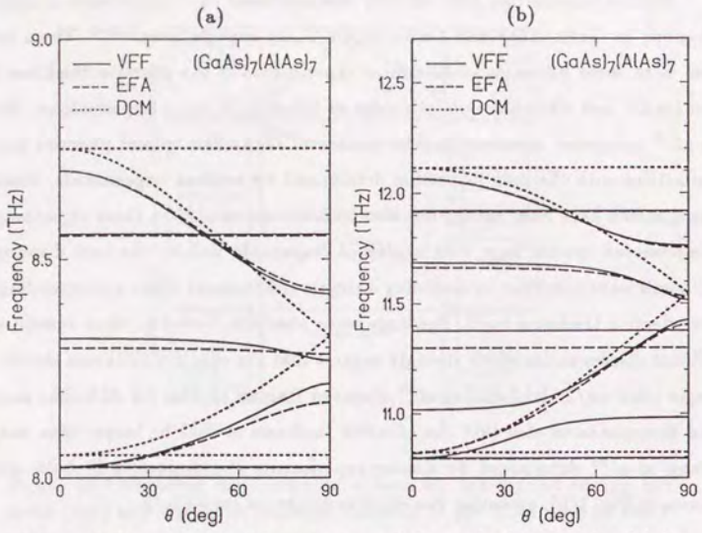

Figure 11 Dependence of the frequency of the modes lying in the vicinity of the LO and TO phonons in bulk GaAs (a) and in bulk AlAs (b) on the wave vector direction at the Γ point. The angle $\theta = 0$ corresponds to the z direction, *i.e.*, [001], and $\theta = \pi/2$ the x direction, *i.e.*, [100]. The solid lines represent the lattice-dynamical results (VFF), the dotted lines those of the conventional dielectric continuum model (DCM), and the dashed lines those of the envelope-function approximation (EFA) to be introduced in Sec. 2-4.

single node is independent of θ. In general, all modes with odd nodes do not exhibit any θ dependence at all. The third mode ($\nu = 8.33$THz at $\theta = 0$) has two nodes, shows a small θ dependence, but interacts strongly with the Fuchs-Kliewer modes at $\theta = \pi/2$. The mode with $\nu = 8.03$THz at $\theta = 0$ is a long-wavelength transverse phonon, *i.e.*, with no node in the GaAs layer. It exhibits a θ dependence quite similar to the lower-branch Fuchs-Kliewer mode. The results for AlAs-like optical modes are shown in Fig. 11(b).

Figures 12 and 13 give corresponding atomic displacements of long-wavelength optical modes with frequencies close to the optical-phonon frequency of bulk GaAs at $\theta = \pi/4$ and $\theta = \pi/2$, respectively. [The displacements at $\theta = 0$ have already

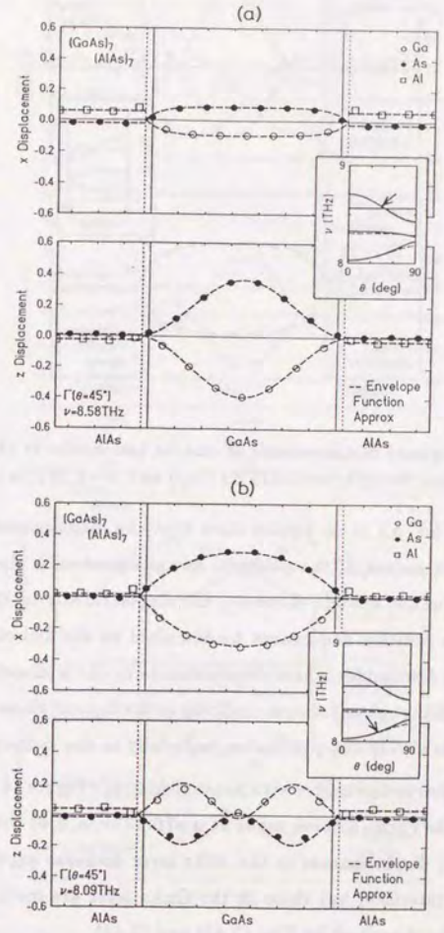

Figure 12 Calculated displacements of ions for two modes at the Γ point and the direction $\theta = \pi/4$. (a) $\nu = 8.58$THz and (b) $\nu = 8.09$THz. The top panel shows displacements in the x direction and the bottom those in the z direction. The displacements in the AlAs layer are nearly independent of z in agreement with the prediction of the dielectric continuum model.

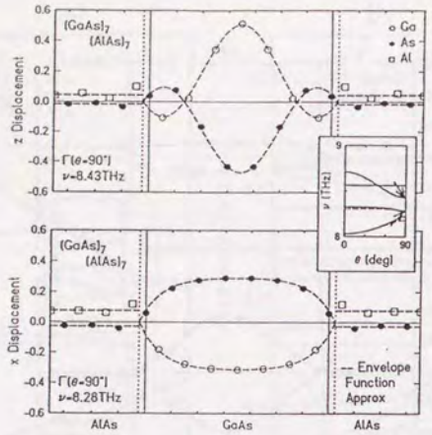

Figure 13 Calculated displacements of ions for two modes at the Γ point and the direction $\theta = \pi/2$. $\nu = 8.43$THz (top) and $\nu = 8.28$THz (bottom).

been given in Fig. 9.] All these figures show that the displacement in the AlAs layer is nearly independent of the position, in agreement with the prediction of the dielectric continuum model. However, the displacements in the GaAs layer strongly depend on position and cannot be described by the dielectric continuum model except for a few modes whose displacements in the x direction are nearly independent of z. Although not shown explicitly in the figures, these modes exhibit small displacements also in the y direction, especially in the vicinity of interfaces.

The same applies to the modes with nonvanishing q_z. Figure 14 gives displacements of a GaAs-like Fuchs-Kliewer mode at $\mathbf{q} = (0.2 \times 2\pi/a, 0, 0)$ with $\nu = 8.30$THz and 8.14THz. The displacements in the AlAs layer decrease exponentially with distance from the interface, but those in the GaAs layer are much more complicated and cannot be described by Eqs. (2.43) and (2.44).

Figure 15 shows displacements of an AlAs-like Fuchs-Kliewer mode at $\mathbf{q} = (0.2 \times 2\pi/a, 0, 0)$ with $\nu = 11.20$THz, which turns out to be quite similar to the GaAs-like modes. Again, it is clear that the results cannot be reproduced by the dielectric continuum model. A more appropriate approximation is highly desirable

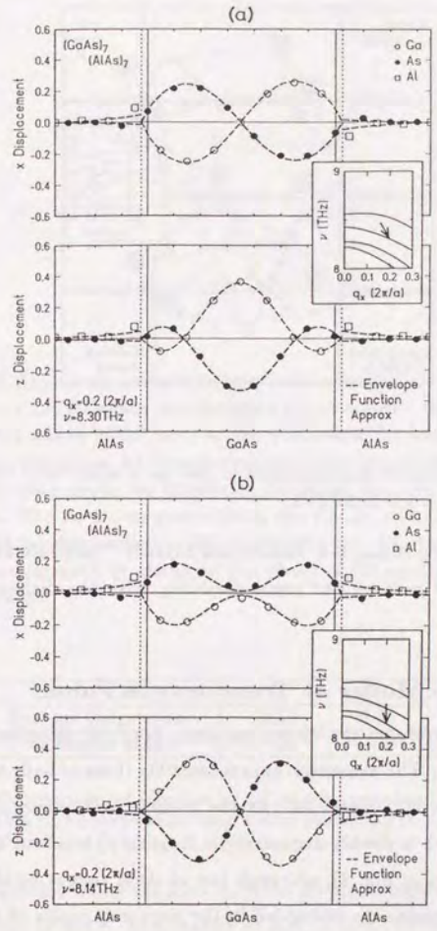

Figure 14 Calculated displacements of ions for two modes with wave vector $(0.2 \times 2\pi/a, 0, 0)$. (a) $\nu = 8.30$THz and (b) $\nu = 8.14$THz. The displacements in the AlAs layer decay exponentially with increasing distance from the interface in agreement with the prediction of the dielectric continuum model. In the GaAs layer, however, they are quite different from those predicted in the dielectric continuum model.

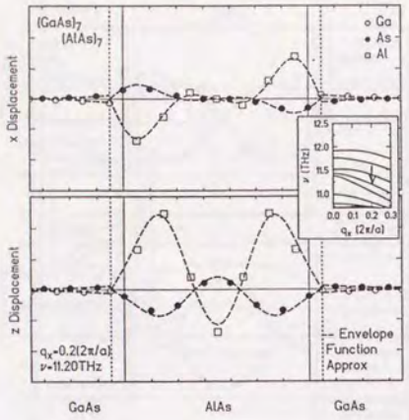

Figure 15 Calculated displacements of ions for a mode with wave vector $(0.2\times 2\pi/a, 0, 0)$. $\nu = 11.20$THz.

and will be introduced in Sec. 2-4. Richter and Strauch[24] made similar comparisons of their results and pointed out some similarity with the dielectric continuum model.

2-3-3 Interface Modes at Transverse X Point

Let us next concentrate on the dispersion along the [100] direction shown in the right panel of Fig. 8. The dispersion curves resemble those of bulk AlAs and GaAs after folding in the [001] direction. At the transverse X point, there are three modes (each of which is doubly degenerate in frequency) localized at the interface (indicated by arrows in Fig. 8), although two of them cannot be identified easily because their frequencies are embedded in the frequency region of other modes.

Figure 16 shows atomic displacements for the isolated mode at 6.75 THz. The displacements are confined in three atomic planes consisting of Ga, interfacial As, and Al. The As ions in the planes sandwiching the three planes remain fixed. This characteristic is applicable to all six interface modes and can be understood in terms of the nature of the tetrahedral bond structure. The Ga and Al atoms

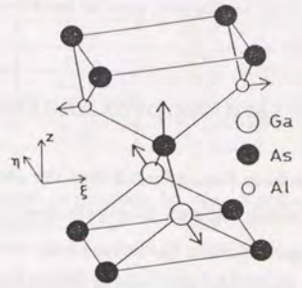

Figure 16 Atomic displacements for a localized interface mode at the X_t point ($\nu = 6.75$THz). The interfacial As atoms move in the [001] direction and the Ga atoms below move in the η direction for which the restoring force from the lowest As layer is smallest. The same is applicable to the Al atoms lying above the interfacial As atoms, *i.e.*, they move in the ξ direction. The As atoms sandwiching the Al, As, and Ga layers exhibit essentially no displacement. Displacements for the other two interface modes are obtained by changing the phase of the oscillations of the Ga and Al atoms.

Interface Mode	1	2	3
Present Calculation	10.25	6.75	2.89
Molecular Model	10.23	6.74	3.00

Table I Comparison of frequencies of interface modes (THz) at the X_t point with a three-plane molecular model consisting of Al, interfacial As, and Ga planes.

move in the direction where the force from the As planes sandwiching the vibrating Ga-As-Al planes is small. As a matter of fact, it turns out that the six interface modes at the transverse X point are well reproduced by a molecular model in which the interfacial As atoms move only in the z direction and the adjacent Ga and Al atoms move only in ξ or η directions, where $\xi = (x+y)/\sqrt{2}$ and $\eta = (-x+y)/\sqrt{2}$. The long-range Coulomb force is not important and may therefore be neglected

completely. Table II compares frequencies calculated in the molecular model with the present results. Finally it is noted that similar interface modes can appear also at other symmetry points.

2-4 Envelope-Function Approximation

In the previous section, it has been demonstrated that the phonons in GaAs/AlAs semiconductor superlattices, which originate from bulk optical phonons of each material, show a complex behavior. Neither the linear-chain model nor the dielectric continuum model alone can reproduce the spectra estimated from a microscopic calculation. As a matter of fact, the linear-chain model is only applicable when the wave vector is perpendicular to the growth direction. The dielectric continuum model, on the other hand, fails to properly describe the confinement of the amplitudes in each layer, although it can successfully describe some features of the interface or Fuchs-Kliewer modes with amplitudes in both layers.

The long-wavelength optical phonons are known to play vital roles in various phenomena involving electron-phonon interactions. Therefore, it is highly desirable to develop an approximation scheme that can fully reproduce the important features of such optical phonons. We propose the following envelope-function approximation:

(i) We employ the continuum approximation in which we consider only the envelope $\mathbf{u}(\mathbf{r})$, which satisfies the equation:

$$(\omega^2 - \omega_{\rm TO}^2)\mathbf{u}(\mathbf{r}) = H(q_x, q_y, \frac{\partial}{i\partial z})\mathbf{u}(\mathbf{r}) - \frac{Ze}{M}\mathbf{E}(\mathbf{r}). \tag{2.46}$$

with $\mathbf{E}(\mathbf{r})$ being the macroscopic electric field determined by the polarization $\mathbf{P}(\mathbf{r})=4(Ze/a^3)\mathbf{u}(\mathbf{r})$ through the integral,

$$\mathbf{E}(\mathbf{r}) = \nabla \int d\mathbf{r}' \frac{\nabla' \cdot \mathbf{P}(\mathbf{r}')}{\epsilon_\infty |\mathbf{r} - \mathbf{r}'|}, \tag{2.47}$$

	A ($\times 10^{-2}$)	B ($\times 10^{-2}$)	C ($\times 10^{-2}$)	$\omega_{\rm TO}$(THz)
GaAs	-1.88	-1.02	-1.64	8.05
AlAs	-1.65	-0.87	-1.37	10.82
GaP	-1.70	-0.92	-1.44	10.95
AlP	-2.17	-1.09	-1.83	13.17
GaSb	-1.52	-0.90	-1.37	6.91
AlSb	-1.04	-0.70	-0.88	9.56

Table III Empirical parameters for the effective Hamiltonian matrix in Eq. (2.48) in units of $\omega_{\rm TO}{}^2 a^2$.

where H is a 3×3 matrix Hamiltonian given by

$$H(q_x, q_y, q_z) = \begin{pmatrix} Aq_x^2+B(q_y^2+q_z^2) & Cq_xq_y & Cq_xq_z \\ Cq_yq_x & Aq_y^2+B(q_z^2+q_x^2) & Cq_yq_z \\ Cq_zq_x & Cq_zq_y & Aq_z^2+B(q_x^2+q_y^2) \end{pmatrix}, \tag{2.48}$$

and M is the reduced mass

$$M = \frac{M_c M_a}{M_c + M_a}. \tag{2.49}$$

The parameters A, B, and C are determined so as to reproduce the bulk dispersions in the long-wavelength limit, calculated by neglecting terms describing macroscopic electric field in the dynamical matrix, *i.e.*, those giving rise to the splitting of LO and TO phonons at the Γ point. For GaAs, we have $A \approx -1.88\times10^{-2}$, $B \approx -1.02\times10^{-2}$, and $C \approx -1.64\times10^{-2}$ in units of $\omega_{\rm TO}^2 a^2$. Parameters for the other materials are given in Table III.

(ii) We neglect the presence of dispersion of phonons in the AlAs layer, *i.e.*, set $A = B = C = 0$ in Eq. (2.48), when calculating GaAs-like optical phonons, and vice versa. This approximation is valid since the amount of dispersion, *i.e.*, the band width, of bulk phonons is smaller than the energy separation between optical phonons in bulk GaAs and AlAs.

(iii) We impose the boundary conditions that the envelopes should vanish at an appropriately chosen boundary plane. As has been discussed in the previous

section, the boundary plane for the GaAs-like modes is chosen at the midpoint of As and Al atomic planes, and that for the AlAs-like modes is chosen at the Ga atomic plane. For practical purposes, such as in discussing electron-phonon interactions, such fine distinctions are not necessary and the boundary plane can be chosen at the interfacial As plane as well.

(iv) A further simplification is obtained by neglecting the anisotropy of the dispersion. The dispersion becomes isotropic when $A=B+C$. Since the anisotropy is small, we may, for example, make the replacement,

$$\begin{aligned} A &\rightarrow A+\delta, \\ B &\rightarrow B-\delta, \\ C &\rightarrow C-\delta, \end{aligned} \tag{2.50}$$

with

$$\delta=(B+C-A)/3, \tag{2.51}$$

to obtain the parameters for an isotropic model. In this simplification, longitudinal and transverse modes are completely decoupled for wave vectors in non-symmetry directions.

The validity of these boundary conditions described in (iii) was carefully examined by Akera and Ando[42] using lattice dynamics. They are easily justified when the wave vector is perpendicular to the layers, because the problem reduces to that of a linear chain. For general directions of the wave vector, the conditions are modified by the presence of a macroscopic electric field, but the effects of such modifications are shown to be negligible for normally confined modes.[42] The only exceptions are the Fuchs-Kliewer or interface modes exhibiting a strong angle dependence at the Γ point. However, these modes are essentially determined by the macroscopic electric field alone and details of the boundary conditions are not important. The detailed explanation of their results is given in Appendix B. Furthermore, the numerical results given in the previous section confirm the validity of these boundary conditions even for the interface modes.

Figures 9–15 already contain the results calculated in the envelope-function approximation. In this calculation, anisotropic phonon dispersion was used. This approximation is not only clearly superior to the simple dielectric continuum model, but it almost exactly reproduces the results calculated directly using the valence-force-field model.

Unfortunately, the present approximation cannot directly be applied to $GaAs/Al_xGa_{1-x}As$ superlattices, which have been subject of many experimental studies on phonons and electron-phonon interactions. In these superlattices, the alloy $Al_xGa_{1-x}As$ layer is known to have two distinct branches of optical phonons, one close to the optical phonon in bulk GaAs and the other close to that in AlAs. So far, only a limited number of theoretical investigations on phonons in such alloy cases have been reported. Arora *et al.*[43] investigated Fuchs-Kliewer modes in the dielectric continuum model in which the $Al_xGa_{1-x}As$ layer has a dielectric function with two poles and two zeros corresponding to the two branches of optical phonons in $Al_xGa_{1-x}As$. Kobayashi and Roy[44] calculated the density of states of several $GaAs/Al_xGa_{1-x}As$ superlattices within a model of nearest- and next nearest-neighbor force constants for large but finite clusters. Jusserand *et al.*[45] calculated phonon modes in a linear-chain model in which the $Al_xGa_{1-x}As$ layer is replaced by a fictitious material having an optical phonon corresponding to the GaAs branch. Babiker[46] proposed a continuum version of this model and extended it to general wave vectors. The validity of such models still remains to be justified, however.

2-5 GaSb/AlSb Superlattices

It has been shown in the previous section that optical phonons in GaAs/AlAs superlattices are well confined to GaAs or AlAs layers except for the presence of interface modes having amplitudes in both layers, and that all long-wavelength phonons are reproduced almost exactly by the envelope-function approximation. These results are a direct consequence of the fact that the frequencies of the optical phonons of the constituent materials do not overlap and are therefore valid in many

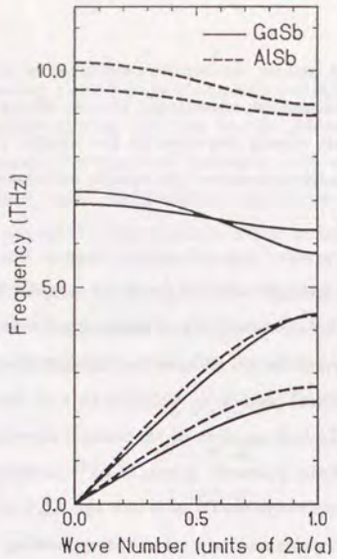

Figure 17 Dispersion relation of phonons in bulk GaSb (solid line) and AlSb (dashed line) in the [001] direction calculated in the valence-force field model with three parameters C_0, C_1, and Z.

different systems which fulfill this condition. As demonstration we investigate strained GaSb/AlSb systems in this section.

The lattice constants of bulk GaSb and AlSb are 6.059 and 6.135 Å, respectively, and their difference, *i.e.*, the lattice mismatch, is 1.2 % and quite large. It is assumed here that in a superlattice grown using these materials, the lattice mismatch between layers is totally accommodated by strain in the layers, so that no misfit defects are generated at the interfaces. The maximum allowable layer thicknesses of such a strained-layer superlattice is a function of the lattice mismatch. A $(GaSb)_7(AlSb)_7$ superlattice, considered in the following, is well below this limit. For simplicity, we assume the lattice constant to be an arithmetic average of GaSb and AlSb and neglect changes in the force constants and effective charges caused by the strain. This approximation is sufficient for the present purpose.

The dispersion relations of bulk GaSb and AlSb in the Γ-Z direction calculated in the valence-force-field model are shown in Fig. 17. Corresponding parameters

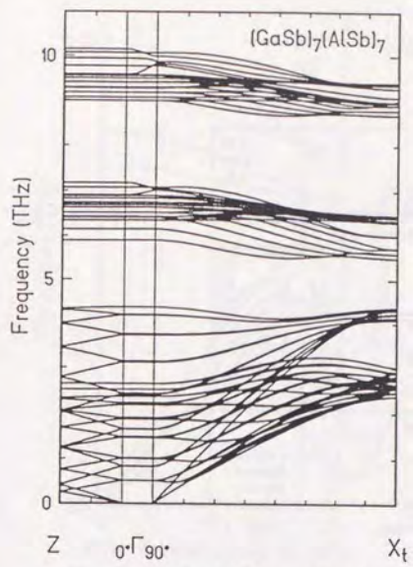

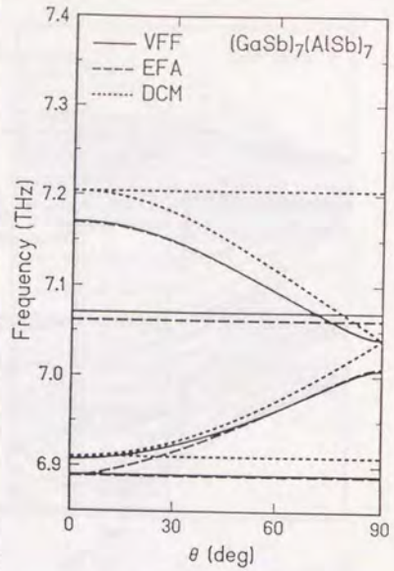

Figure 18 (left) Calculated phonon dispersion relation in a $(GaSb)_7$ $(AlSb)_7$ superlattice grown in the [001] direction.

Figure 19 (right) Dependence of frequency for modes lying in the vicinity of LO and TO phonons in bulk GaSb on the wave vector direction at the Γ point.

are given in Table I. As is clearly seen in the figure, the frequency of optical phonons is much larger in AlSb than in GaSb.

Figure 18 shows the calculated dispersion relation of a $(GaSb)_7(AlSb)_7$ superlattice. The results have the same features as those of GaAs/AlAs, *i.e.* the presence of four direction-dependent interface modes and the confinement of all optical modes in either GaSb or AlSb layers. Figure 19 gives the θ dependence of optical modes with frequency close to that of optical phonons in bulk GaSb together with the results calculated in the envelope-function approximation and the dielectric continuum model. Figure 20 gives the displacements due to a GaSb-like optical mode at $\mathbf{q} = (0.2 \times 2\pi/a, 0, 0)$ with $\nu = 6.88$THz calculated in lattice-dynamics and the envelope-function approximation. All these results show clearly that the envelope-function approximation reproduces the lattice-dynamical results

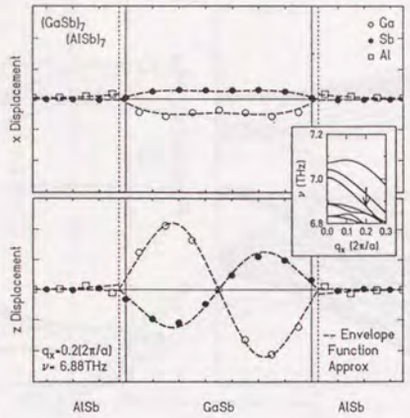

Figure 20 Calculated displacements of ions for a mode with wave vector $(0.2\times 2\pi/a, 0, 0)$ in a $(GaSb)_7(AlSb)_7$ superlattice. $\nu = 6.88$THz.

almost exactly. The same holds for AlSb-like modes, though the results are not shown here.

2-6 GaP/AlP Superlattices

There are superlattice systems for which optical-phonon frequencies of constituent materials do overlap. One typical example is GaSb/InAs for which TO frequencies at the Γ point are quite close because the reduced mass of GaSb and that of InAs are almost equal. In this case the connection of the envelopes of lattice displacements of adjacent layers at interfaces must be considered carefully. Akera and Ando[42] described the connection rules in terms of a set of linear relations between the envelopes and their first z derivatives of both materials and obtained explicit results in the valence-force-field model. In this section we consider the GaP/AlP systems which is different from both GaAs/AlAs and GaSb/InAs. The lattice mismatch between these materials is only 0.2 % and can be neglected.

Figure 21 shows the dispersion relations along the Γ-Z direction of bulk GaP and AlP calculated in the valence-force-field model for the parameters listed in

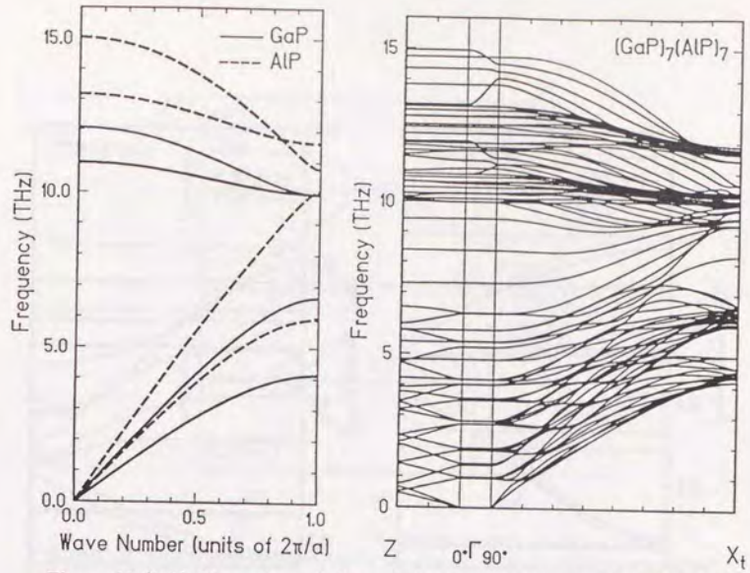

Figure 21 (left) Dispersion relation of phonons in bulk GaP (solid line) and AlP (dashed line) in the [001] direction calculated in the valence-force field model.

Figure 22 (right) Calculated phonon dispersion relation in a $(GaP)_7(AlP)_7$ superlattice grown in the [001] direction.

Table I. The frequencies of optical phonons of these materials partly overlap each other, *i.e.*, both ω_{LO} and ω_{TO} of AlP are embedded in the frequency range of bulk GaP optical phonons in the vicinity of the X point. Further, there is a wide frequency interval where only LA phonons of AlP (TA phonons of GaP) are present but those of GaP (AlP) are not.

Figure 22 gives the dispersion relation of a $(GaP)_7(AlP)_7$ superlattice calculated in lattice dynamics. Along the Γ-Z direction, in the left panel, some optical modes exhibit dispersion because of the partial overlap of the frequencies of bulk optical phonons. It is difficult to determine whether each optical mode is GaP-like or AlP-like. LA modes between 7 and 10THz exhibit no dispersion and are confined to the AlP layer, because there are no longitudinal modes in GaP in this frequency region. Below 7THz, all LA modes exhibit dispersion and are extended

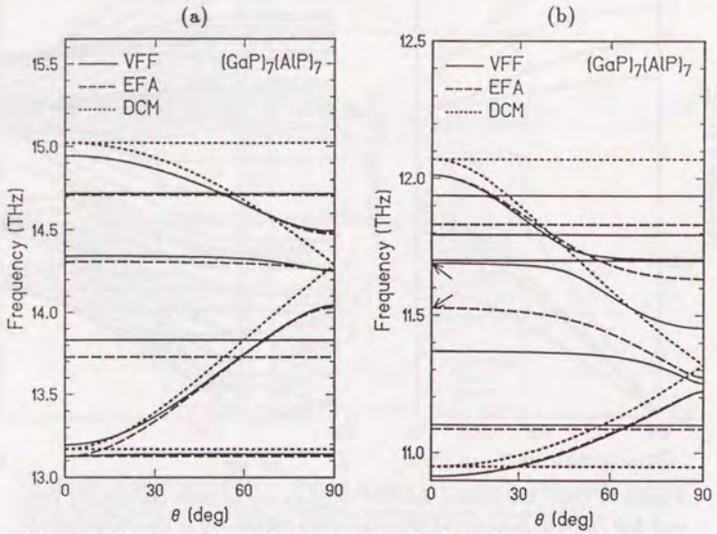

Figure 23 Dependence of frequency of modes lying in the vicinity of ω_{LO} and ω_{TO} of AlP (a) and GaP (b) on the wave vector direction at the Γ point.

over both layers. The behavior of the TA modes is qualitatively the same as the LA modes.

Figure 23(a) shows the θ dependence of the optical modes with frequency close to that of the optical phonons in bulk AlP together with the results calculated in the envelope-function approximation and the dielectric continuum model. For modes with frequencies close to the optical phonons of bulk AlP, the envelope-function approximation reproduces the lattice-dynamical results almost exactly. Displacements of ions of an AlP-like optical mode at $\mathbf{q}=(0.2\times 2\pi/a, 0, 0)$ with $\nu=$ 13.94THz calculated in lattice-dynamics and the envelope-function approximation are shown in Fig. 24. The envelope-function approximation again reproduces the result obtained in lattice-dynamics almost exactly.

Figure 23(b) compares the θ dependence for modes with frequency close to ω_{LO} and ω_{TO} of GaP. Because ω_{LO} of GaP lies above the frequency of the LO phonon of AlP at the X point, the θ dependence obtained by the lattice-dynamical

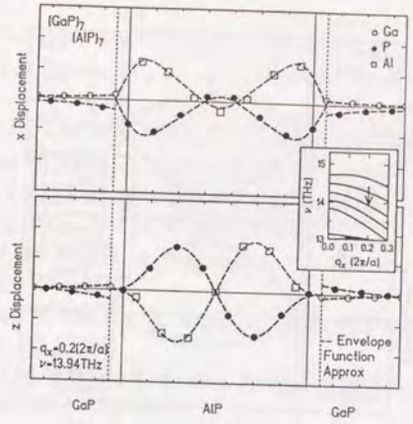

Figure 24 Calculated displacements of ions for a mode with wave vector $(0.2\times 2\pi/a, 0, 0)$ in a $(GaP)_7(AlP)_7$ superlattice. $\nu=13.94$THz.

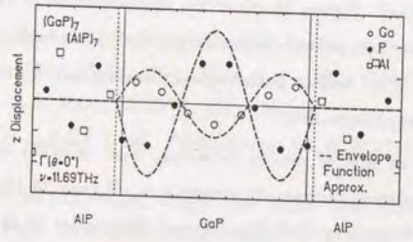

Figure 25 Calculated displacements of ions for LO modes at the Γ point denoted by the arrows in Fig. 23(b). They are not confined to either GaP or AlP layers .

calculation is quite complicated and cannot be reproduced well by the envelope-function approximation. As a matter of fact, the number of modes lying between ω_{LO} and ω_{TO} of GaP is ten in the lattice dynamics (some modes are degenerate) in contrast to five in the envelope-function approximation. Five extra modes come from LO and TO phonons of AlP in the vicinity of the X point which are coupled

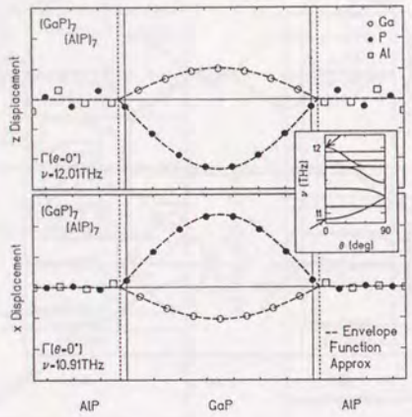

Figure 26 Calculated displacements of ions for the highest-energy LO mode (top) and TO mode (bottom) of GaP-like optical modes at the Γ point.

to LO phonons of GaP. Figure 25 gives the displacements of the ions of a mode which has a character of confined modes in the GaP layer and an X-like character in the AlP layer. This rather pathological case cannot be reproduced by the envelope-function approximation.

Apart from such special modes, however, most of other modes are well described by the envelope-function approximation. Figure 26 shows displacements of ions for highest frequency GaP-like LO and TO modes at the Γ point at $\theta = 0$. For the LO phonon, the envelope-function approximation can describe the lattice-dynamical result quite well except in the AlP layer. For the TO phonon, on the other hand, the agreement is nearly perfect. The overlap of TO phonon spectra of GaP and AlP is small and negligible owing to the their small dispersions.

References

1. R. Tsu and S.S. Jha, Appl. Phys. Lett. **20**, 16 (1972).
2. J.L. Merz, A.S. Barker, Jr., and A.C. Gossard, Appl. Phys. Lett. **31**, 117 (1977).
3. A.S. Barker, Jr., J.L. Merz, and A.C. Gossard, Phys. Rev. B **17**, 3181 (1978).
4. N. Sawaki and N. Akasaki, Physica **134B**, 494 (1985).
5. C. Colvard, T.A. Gant, M.V. Klein, R. Merlin, R. Fischer, H. Morkoç, and A.C. Gossard, Phys. Rev. B **31**, 2080 (1985).
6. B. Jusserand, D. Paquet, A. Regreny, and J. Kervarec, J. Phys. (Paris) Colloq. **45**, C5-145 (1984).
7. M. Nakayama, K. Kubota, H. Kato, S. Chika, and N. Sano, Solid State Commun. **53**, 493 (1985).
8. M. Nakayama, K. Kubota, K. Kanata, H. Kato, S. Chika, and N. Sano, Jpn. J. Appl. Phys. **24**, 1331 (1985).
9. B. Zhu and K.A. Chao, Phys. Rev. B **36**, 4906 (1987).
10. See for example, C. Kittel, *Introduction to Solid State Physics*, 5th ed. (Wiley, New York, 1976), p. 105.
11. S.M. Rytov, Sov. Phys. Acous. **2**, 68 (1956).
12. C. Colverd, R, Merlin, M.V. Klein, and A.C. Gossard, Appl. Phys. Lett. **43**, 298 (1980).
13. J. Sapriel, B. Djafari-Rouhani, and L. Dobrzynski, Surf. Sci. **126**, 197 (1983).
14. S. Tamura and J.P. Wolfe, Phys. Rev. B **35**, 2528 (1987).
15. S.M. Rytov, Sov. Phys. JETP **2**, 466 (1956).
16. E.P. Pokatilov and S.I. Beril, Phys. Status Solidi B **110**, K75 (1982); **118**, 567 (1983).
17. R.E. Camley and D.L. Mills, Phys. Rev. B **29**, 1695 (1984).
18. R. Lassnig, Phys. Rev. B **30**, 7132 (1984).
19. M. Nakayama, M. Ishida, and N. Sano, Phys. Rev. B **38**, 6348 (1988).
20. R. Fuchs and K.L. Kliewer, Phys. Rev. **140**, A2076 (1965).
21. T. Tsuchiya, H. Akera, and T. Ando, Phys. Rev. B **39**, 6025 (1989).
22. S.K. Yip and Y.C. Chang, Phys. Rev. B **30**, 7037 (1984).
23. T. Toriyama, N. Kobayashi, and Y. Horikoshi, Jpn. J. Appl. Phys. **25**, 1895 (1986).
24. E. Richter and D. Strauch, Solid State Commun. **64**, 867 (1987).
25. S.F. Ren, H. Chu, and Y.C. Chang, Phys. Rev. Lett. **59**, 1841 (1987); Phys. Rev. B **37**, 8899 (1988).

26. H. Chu, S.F. Ren, and Y.C. Chang, Phys. Rev. B **37**, 10746 (1988).

27. K. Huang and B.F. Zhu, Phys. Rev. B **38**, 2183 (1988) ; Phys. Rev. B **38**, 13377 (1988).

28. M.V. Klein, IEEE J. Quantum Electron. **QE-22**, 1760 (1986).

29. B. Jusserand and D. Paquet, in *Semiconductor Heterostructures and Superlattices*, ed. by G. Allan *et al.*(Springer, Berlin, 1986), p. 108.

30. J. Sapriel and B. Djaferi-Rouhani, Surf. Sci. Rep. **10**, 189 (1989).

31. J. Menéndez, J. Luminescence **44**, 285 (1989).

32. B. Jusserand, Ann. Phys. Fr. **13**, 597 (1988).

33. D.L. Mills, in *Light Scattering In Solids V*, ed. by M. Cardona, and G. Güntherodt (Springer, Berlin, 1989), p. 13.

34. B. Jusserand and M. Cardona, in *Light Scattering In Solids V*, ed. by M. Cardona and G. Güntherodt (Springer, Berlin, 1989), p. 49.

35. A. Mooradian and G.B. Wright, Solid State Commun. **4**, 431 (1966).

36. J.L.T. Waugh and G. Dolling, Phys. Rev. **132**, 2410 (1963).

37. A. Onton, in *Proceedings of the 10th International Conference on the Physics of Semiconductors, Cambridge, 1970*, edited by S.P. Keller, J.C. Hensel, and F. Stern (the United States Atomic Energy Commission, Division of Technical Information, Oak Ridge, 1970), p. 107.

38. Z.P. Wang, D.S. Jiang, and K. Ploog, Solid State Commun. **65**, 661 (1988).

39. B. Jusserand and D. Paquet, Phys. Rev. Lett. **56**, 1752 (1986).

40. A.K. Sood, J. Menéndez, M. Cardona, and K. Ploog, Phys. Rev. Lett. **54**, 2111 (1985); **56**, 1753 (1986).

41. A. Ishibashi, M. Itabashi, Y. Mori, K. Kaneko, S. Kawado, and N. Watanabe, Phys. Rev. B **33**, 2887 (1986).

42. H. Akera and T. Ando, Phys. Rev. B **40**, 2914 (1989).

43. A.K. Arora, A.K. Ramdas, M.R. Melloch, and N. Otsuka, Phys. Rev. B **36**, 1021 (1987).

44. A. Kobayashi and A. Roy, Phys. Rev. B **35**, 2237 (1987).

45. B. Jusserand, D. Paquet, and A. Regreny, Phys. Rev. B **30**, 6245 (1984).

46. M. Babiker, J. Phys. C **19**, 683 (1986).

Chapter 3

Electron-Phonon Interaction

3-1 Electron-Phonon Scattering

3-1-1 Polaron Damping and Inter-Subband Relaxation

The scattering rate of an electron in subband η $(= 1, 2 \ldots)$ at wave vector $\mathbf{k}$ to subband η' by phonon emission and absorption is represented by Fermi's golden rule as

$$\frac{1}{\tau_{\eta,\eta',\pm}(\mathbf{k})} = \frac{2\pi}{\hbar}\frac{V}{(2\pi)^3}\sum_j\sum_{\eta'}\int d\mathbf{q}|M(j,\eta,\eta';\mathbf{k},\mathbf{q})|^2 \times\left[n(\omega_j(q))+\frac{1}{2}\pm\frac{1}{2}\right]\delta(E_f - E_i \pm \hbar\omega_j(q)), \tag{3.1}$$

with

$$n(\omega) = \left[\exp(\frac{\hbar\omega}{k_BT})-1\right]^{-1}, \tag{3.2}$$

where M is the matrix element of electron-phonon interaction, V $(= L^3)$ is a volume of the system, $\omega_j(q)$ is the frequency of an optical phonon of mode j and wave vector $\mathbf{q}$, E_i and E_f are the electron energies of initial and final states, respectively, k_B is the Boltzmann constant, and T is the temperature. The upper and lower signs represent the contributions of phonon emission and absorption processes, respectively. The matrix element M can be expressed as

$$M(j,\eta,\eta';\mathbf{k},\mathbf{q}) = \int d\mathbf{r}\psi^*_{\eta',\mathbf{k}\mp\mathbf{q}}(\mathbf{r})H_i(j,\mathbf{q};\mathbf{r})\psi_{\eta,\mathbf{k}}(\mathbf{r}), \tag{3.3}$$

where the interaction Hamiltonian H_i is written as

$$H_i(j,\mathbf{q};\mathbf{r}) = -e\Phi(j,\mathbf{q};\mathbf{r}) \tag{3.4}$$

where Φ is the potential associated with lattice displacement.

We assume that an electron is completely confined to the well layers and adopt the wave function

$$\psi_{\eta,\mathbf{k}}(\mathbf{r}) = \frac{1}{\sqrt{N}}\sum_{l=1}^{N}\theta_1(z)\sqrt{\frac{2}{d_1}}\sin\Big(\frac{\eta\pi}{d_1}(z-ld)\Big)\exp(ik_z ld)\,\frac{\exp(i\mathbf{k}_{||}\cdot\mathbf{r}_{||})}{L}, \tag{3.5}$$

with

$$\theta_1 = \begin{cases} 1 & \text{in layer 1} \\ 0 & \text{otherwise,} \end{cases} \tag{3.6}$$

where d_1 is thickness of well layers, d $(=d_1+d_2)$ is the period of the superlattice, l $(=1,2\ldots N)$ is the layer index, N $(=L/d)$ is the number of the layers, $\mathbf{k}=(\mathbf{k}_{||},k_z)$, and $\mathbf{r}=(\mathbf{r}_{||},z)$. The corresponding energy is

$$E_\eta(\mathbf{k}_{||}) = \frac{\hbar^2}{2m^*}\left(\frac{\pi}{d_1}\eta\right)^2 + \frac{\hbar^2 k_{||}^2}{2m^*}, \tag{3.7}$$

where m^* is the effective mass. This assumption is valid when the thickness of the barrier and well layers is sufficiently large. For GaAs/AlAs systems, the critical thickness is quite small (estimated as ~ 30 Å using the effective-mass approximation) because of the large discontinuity of the conduction band (~ 1 eV).

In general, the polaron damping rate depends on the initial energy of the electron E. However, as shown in the numerical estimation by Mason and Das Sarma[1], its dependence is small. Thus we neglect its dependence and evaluate it at $E=0$. Namely, we calculate the damping rate for the electron at the bottom of the ground subband due to LO phonon absorption. Figure 1(a) illustrates this process. If the splitting between the ground and first excited subbands is larger than the phonon energy, there are no inter-subband processes. Therefore it can be calculated from Eq. (3.1) with $M(j,1,1;0,\mathbf{q})$ and $E_f-E_i=\hbar^2 q_{||}^2/2m^*$. We shall calculate also an

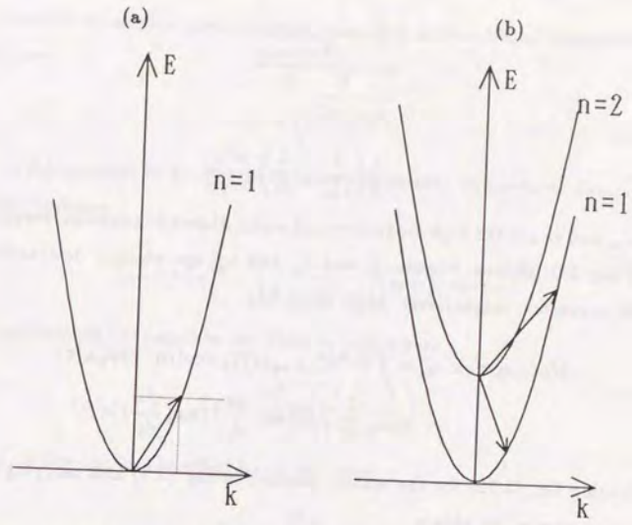

Figure 1 Processes of (a) polaron damping and of (b) inter-subband relaxation. n is a subband index.

inter-subband relaxation rate corresponding to scattering of an electron at the bottom of the first excited subband to the ground subband. There are both phonon emission and absorption processes as illustrated in Figure 1(b). These rates can be calculated by Eq. (3.1) with $M(j,2,1;0,\mathbf{q})$ and $E_f-E_i=E_1(q_{||})-E_2(0)$. The damping rate Γ is related to the corresponding relaxation time τ defined in Eq. (3.1) through $\Gamma=\hbar/2\tau$.

3-1-2 Bulk-Phonon Model

The simplest approximation is to use phonons of the bulk material forming the well layer. The interaction with LO phonons is described by the Fröhlich Hamiltonian

$$H_I(\mathbf{r}) = \sum_{\mathbf{q}} V_{\mathbf{q}}\Big[b_{\mathbf{q}}^{\dagger}\exp(-i\mathbf{q}\cdot\mathbf{r}) - b_{\mathbf{q}}\exp(i\mathbf{q}\cdot\mathbf{r})\Big], \tag{3.8}$$

with

$$V_{\mathbf{q}} = -i\frac{\hbar\omega_{\mathrm{LO}}}{|\mathbf{q}|\sqrt{u}}\left(\frac{4\pi\alpha_F}{V}\right)^{1/2}, \tag{3.9}$$

$$u = \sqrt{\frac{2m^*\omega_{\rm LO}}{\hbar}}, \tag{3.10}$$

and

$$\alpha_F = \frac{1}{2}\left(\frac{1}{\epsilon_\infty} - \frac{1}{\epsilon_0}\right)\frac{e^2 u}{\hbar\omega_{\rm LO}}, \tag{3.11}$$

where ϵ_∞ and ϵ_0 are the high-frequency and static dielectric constant, respectively, $\omega_{\rm LO}$ is the LO phonon frequency, and $b_{\mathbf{q}}$ and $b_{\mathbf{q}}^+$ are phonon destruction and creation operators, respectively. More explicitly

$$\begin{aligned} M_B(j,\eta,\eta';\mathbf{k},\mathbf{q}) &= \int d\mathbf{r}^3 \psi^*_{\eta',\mathbf{k}+\mathbf{q}}(\mathbf{r}) V_{\mathbf{q}} \exp(i\mathbf{q}\cdot\mathbf{r})\psi_{\eta,\mathbf{k}}(\mathbf{r}) \\ &= V_{\mathbf{q}}\,\frac{2}{d_1}\int dz \sin(\frac{\eta\pi}{d_1}z)\sin(\frac{\eta'\pi}{d_1}z)e^{iq_z z} \end{aligned} \tag{3.12}$$

Substituting Eq. (3.12) for the matrix element in Eq. (3.1) and carrying out the integration over $\mathbf{q}$, we obtain

$$\Gamma_{\eta,\eta'} = \frac{\pi m^*\omega_{\rm LO}e^2}{\hbar q_0}\left(\frac{1}{\epsilon_\infty} - \frac{1}{\epsilon_0}\right)\left[n(\omega_{\rm LO}) + \frac{1}{2} \pm \frac{1}{2}\right] I_{\eta,\eta'}(q_0), \tag{3.13}$$

with

$$\begin{aligned} I_{\eta,\eta'}(q_0) = \frac{2}{d_1^2}\int_0^{d_1} dz \int_0^{d_1} dz' e^{-q_0|z-z'|} \\ \times \sin(\frac{\eta\pi}{d_1}z)\sin(\frac{\eta'\pi}{d_1}z)\sin(\frac{\eta\pi}{d_1}z')\sin(\frac{\eta'\pi}{d_1}z'), \end{aligned} \tag{3.14}$$

where we have used the identity

$$\int_{-\infty}^{\infty} dq_z \frac{e^{iq_z(z-z')}}{q_0^2 + q_z^2} = \pi\frac{e^{-q_0|z-z'|}}{q_0} \tag{3.15}$$

and q_0 denotes $|\mathbf{q}_{||}|$ satisfying energy conservation. The integration of Eq. (3.14) can be carried out analytically[2] and yields

$$\begin{aligned} I_{\eta,\eta'}(q_0) = q_0 d_1 \Bigg[&\frac{(1+\delta_{\eta,\eta'}/2)(q_0d_1)^2 + (1+\delta_{\eta,\eta'})(\eta^2+\eta'^2)\pi^2}{[(q_0d_1)^2 + (\eta+\eta')^2\pi^2][(q_0d_1)^2 + (\eta-\eta')^2\pi^2]} \\ &+ q_0d_1\{(-1)^{\eta+\eta'}e^{-q_0d_1} - 1\} \\ &\times \left\{\frac{4\eta\eta'\pi^2}{[(q_0d_1)^2 + (\eta+\eta')^2\pi^2][(q_0d_1)^2 + (\eta-\eta')^2\pi^2]}\right\}^2\Bigg]. \end{aligned} \tag{3.16}$$

We shall investigate some limiting cases. For intra-subband transitions ($\eta' = \eta$), we have

$$q_0 = \sqrt{\frac{2m^*\omega_{\rm LO}}{\hbar}}, \tag{3.17}$$

which is independent of d_1. For small layer thicknesses, the polaron damping rate therefore becomes

$$\Gamma_{\eta,\eta} \to \Gamma_0\left[1 - \left(\frac{1}{3} - \frac{5}{4\eta^2\pi^2}\right)(q_0d_1)\right] n(\omega_{\rm LO}), \tag{3.18}$$

which approaches $\Gamma_0 n(\omega_{\rm LO})$ in the limit $d_1 \to 0$, where

$$\Gamma_0 = \frac{\pi e^2}{4} q_0 \left(\frac{1}{\epsilon_\infty} - \frac{1}{\epsilon_0}\right). \tag{3.19}$$

When $d_1 \gg 2\eta\pi/q_0$, on the other hand, we have

$$\Gamma_{\eta,\eta} = \frac{3\Gamma_0}{q_0 d_1} n(\omega_{\rm LO}), \tag{3.20}$$

which decreases as d_1^{-1}.

For inter-subband transitions, q_0 depends on d_1. For narrow wells where the subband splitting

$$\Delta E_{\eta,\eta'} = \frac{\hbar^2}{2m^*}\left(\frac{\pi}{d_1}\right)^2 |\eta^2 - \eta'^2| \tag{3.21}$$

is much larger than the LO phonon energy, we have

$$q_0 \cong \frac{\pi}{d_1}\sqrt{|\eta^2 - \eta'^2|}. \tag{3.22}$$

and

$$\begin{aligned} \Gamma_{\eta,\eta'} = &d_1 \frac{\pi m^*\omega_{\rm LO}e^2}{\hbar}\left(\frac{1}{\epsilon_\infty} - \frac{1}{\epsilon_0}\right)\left[n(\omega_{\rm LO}) + \frac{1}{2} \pm \frac{1}{2}\right] \\ &\times \Bigg\{\frac{1}{2\pi^2|\eta^2 - \eta'^2|} + \pi\sqrt{|\eta^2 - \eta'^2|}\left[(-1)^{\eta+\eta'}e^{-\pi\sqrt{|\eta^2-\eta'^2|}} - 1\right] \\ &\times \left[\frac{4\eta\eta'}{\pi^2\left[|\eta^2 - \eta'^2| + (\eta+\eta')^2\right]\left[|\eta^2 - \eta'^2| + (\eta-\eta')^2\right]}\right]^2\Bigg\}. \end{aligned} \tag{3.23}$$

Therefore, the inter-subband scattering rate is proportional to the layer thickness for narrow layers. With increasing layer thickness, q_0 becomes larger than Eq. (3.22) for absorption processes and smaller for emission processes. Because $\Gamma_{\eta\eta'}$ is a decreasing function of q_0, $\Gamma_{\eta\eta'}$ for absorption increases sub-linearly and that for emission increases super-linearly with d_1.

3-1-3 Dielectric Continuum Model

As shown in Sec. 2-1-3, there are two kinds of modes in the dielectric continuum model, infinitely degenerate "confined modes" and four "interface modes." The potential due to the confined modes are described as

$$\Phi_{C,n,\mathbf{q}}(\mathbf{r}) = \frac{1}{\sqrt{N}}\sum_{l=1}^{N} a_{C,n}\sqrt{\frac{2}{d_1}}\sin\left[\frac{n\pi}{d_1}(z-ld)\right]e^{iq_z ld}\frac{e^{i\mathbf{q}_\parallel\cdot\mathbf{r}_\parallel}}{L}\theta_l b_{C,n,\mathbf{q}} + h.c., \tag{3.24}$$

where the subscript C denotes the confined modes and $\theta_l = 1$ in layer l and 0 in the other layer. Because the confined modes in layer 2 do not induce any potential in layer 1, they do not couple with electrons confined to layer 1.

The normalization factor $a_{C,n}$ is determined in such a way that the energy expectation value of each mode is equal to its eigen energy. It is straightforward to calculate the expectation value by using the lattice displacement determined by Eq. (2.26) and a virial theorem. The result is

$$a_{C,n} = \left\{\frac{\hbar}{2\omega_{\mathrm{LO}}\left[q_\parallel^2 + (\frac{n\pi}{d_1})^2\right]\beta^2(\omega_{\mathrm{LO}})}\right\}^{\frac{1}{2}}, \tag{3.25}$$

with

$$\beta(\omega) = \frac{\left[\frac{\epsilon_\infty}{4\pi}(\omega_{\mathrm{LO}}^2 - \omega_{\mathrm{TO}}^2)\right]^{1/2}}{\omega^2 - \omega_{\mathrm{TO}}^2}. \tag{3.26}$$

From Eqs. (3.3), (3.4), (3.5), and (3.24), we obtain

$$M_C(n,\eta,\eta';\mathbf{k},\mathbf{q}) = \frac{ea_{C,n}}{N^{1/2}L}\left(\frac{2}{d_1}\right)^{1/2} \times\left(-\frac{1}{\pi}\right)\frac{8\eta\eta' n}{\{(\eta+\eta')^2+n^2\}\{(\eta-\eta')^2+n^2\}} \tag{3.27}$$

for $\eta+\eta'+n=$ odd and $M_C(n,\eta,\eta';\mathbf{k},\mathbf{q}) = 0$ for $\eta+\eta'+n=$ even. Substitution of this equation into Eq. (3.1) and integration over $\mathbf{q}$ gives

$$\Gamma_{C;\eta,\eta'} = \frac{\pi m^* \omega_{\mathrm{LO}} e^2}{\hbar q_0}\left(\frac{1}{\epsilon_\infty}-\frac{1}{\epsilon_0}\right)\left[n(\omega_{\mathrm{LO}})+\frac{1}{2}\pm\frac{1}{2}\right] \times\sum_{n(\eta+\eta'+n=\mathrm{odd})}\frac{2}{\pi^2}\frac{q_0 d_1}{(q_0 d_1)^2+(n\pi)^2}\left[\frac{8\eta\eta' n}{\{(\eta+\eta')^2+n^2\}\{(\eta-\eta')^2+n^2\}}\right]^2. \tag{3.28}$$

Let us consider some limiting cases. For intra-subband transitions $\eta' = \eta$, the summation over n in Eq. (3.28) is dominated by the term with $n=1$ because of the presence of a factor proportional to n^{-2}. We have the following approximate expression:

$$\Gamma_{C;\eta,\eta} = \frac{\pi m^* \omega_{\mathrm{LO}} e^2}{\hbar q_0}\left(\frac{1}{\epsilon_\infty}-\frac{1}{\epsilon_0}\right)\left[n(\omega_{\mathrm{LO}})+\frac{1}{2}\pm\frac{1}{2}\right] \times\frac{128}{\pi^2}\frac{q_0 d_1}{(q_0 d_1)^2+\pi^2}\frac{\eta^4}{(4\eta^2+1)^2}. \tag{3.29}$$

This expression immediately shows that, with increasing layer thickness, the damping rate increases in proportion to the thickness, has a maximum around $d_1 \sim \pi/q_0$, and decreases in proportion to the inverse of the layer thickness when $q_0 d_1 \gg 1$. The vanishing damping rate for vanishing layer thickness is a direct consequence of the divergence of the effective phonon wavenumber, given by $\sqrt{q_0^2+(\pi/d_1)^2}$, due to the confinement in the layer.

For inter-subband transitions, a simplified expression can be given in the limit of narrow layers. In this limit, q_0 is determined by Eq. (3.22) and $q_0 d_1$ is independent of d_1. Then, the damping rate is given by

$$\Gamma_{C,\eta,\eta'} = d_1\gamma_1\left(\frac{1}{\epsilon_\infty}-\frac{1}{\epsilon_0}\right)\left[n(\omega_{\mathrm{LO}})+\frac{1}{2}\pm\frac{1}{2}\right] \times\sum_n\frac{2}{\pi^2}\frac{1}{\pi^2|\eta^2-\eta'^2|+n^2\pi^2}\left\{\frac{8\eta\eta' n}{[(\eta+\eta')^2+n^2][(\eta-\eta')^2+n^2]}\right\}, \tag{3.30}$$

which is proportional to the layer thickness. There will be deviations from this linear dependence with increasing layer thickness as discussed at the end of Sec. 3-1-2.

Next, let us consider the contributions of the interface modes. Choosing $\mathbf{r}_{||}$ in the direction of $\mathbf{q}_{||}$, we have

$$\begin{aligned}\Phi_{\mathrm{IF},j}(\mathbf{r},\mathbf{q}) =& \frac{a_{I,j,\mathbf{q}}}{N^{1/2}} \sum_{l=1}^{N} e^{iq_z ld} \frac{e^{iq_{||}r_{||}}}{L} \\ &\times \Big[\Big\{ C_{S,1,j} \cosh[q_{||}(z-ld-\frac{d_1}{2})]\theta_1 \\ &+ C_{A,1,j} \sinh[q_{||}(z-ld-\frac{d_1}{2})]\theta_1 \\ &+ C_{S,2,j} \cosh[q_{||}(z-ld-d_1-\frac{d_2}{2})]\theta_2 \\ &+ C_{A,2,j} \sinh[q_{||}(z-ld-d_1-\frac{d_2}{2})]\theta_2 \Big\} b_{I,j,\mathbf{q}} + h.c. \Big],\end{aligned} \tag{3.31}$$

where j is mode index and the coefficients $C_{S,1,j}$ *etc.* are determined by Eq. (2.38). The normalization $a_{I,j,\mathbf{q}}$ is calculated as

$$\begin{aligned}a_{I,j,\mathbf{q}} = \Big\{ 2\omega_{j,\mathbf{q}} q_{||} \big[&(C_{S,1,j}^2 + C_{A,1,j}^2)\beta_1^2(\omega_j(\mathbf{q})) \sinh(q_{||}d_1) \\ &+ (C_{S,2,j}^2 + C_{A,2,j}^2)\beta_2^2(\omega_j(\mathbf{q})) \sinh(q_{||}d_2) \big] \Big\}^{-1/2},\end{aligned} \tag{3.32}$$

where $\beta_1(\omega)$ and $\beta_2(\omega)$ are defined by Eq. (3.26) for ω_{LO} and ω_{TO} of layer 1 and 2, respectively. The corresponding matrix element is given by

$$\begin{aligned}M_{\mathrm{IF}}(\eta,\eta';j) =& \frac{e a_{I,j,\mathbf{q}} \sqrt{d_1+d_2}\, q_{||} d_1}{\sqrt{V}} \Big[\frac{1}{(q_{||}d_1)^2+(\eta-\eta')^2\pi^2} - \frac{1}{(q_{||}d_1)^2+(\eta+\eta')^2\pi^2} \Big] \\ &\times \Big[C_{S,1,j}((-1)^{\eta+\eta'}+1)\sinh(\frac{q_{||}d_1}{2}) + C_{A,1,j}((-1)^{\eta+\eta'}-1)\cosh(\frac{q_{||}d_1}{2}) \Big].\end{aligned} \tag{3.33}$$

Note that the normalization of the C's is arbitrary and the final results do not depend on the normalization.

We do not write out explicit analytical formulas in the limiting cases $q_{||}d_1 \ll 1$ and $q_{||}d_1 \gg 1$, since the C's are a complicated function of the wave vector, d_1, and d_2. Instead, we confine ourselves to the case that $d_1 = d_2$ where C's are independent of d_1 which simplifies the expressions. For intra-subband transitions, both matrix element M_{IF} and damping rate approach a constant in the limit of narrow layers, $q_0 d_1 \ll 1$. In the limit of wide layers we have $M_{\mathrm{IF}} \propto d_1^{-5/2}$, which

shows that the damping rate decreases in proportion to d_1^{-5}. For inter-subband transitions and in the limit of narrow layers, $q_0 d_1$ becomes independent of d_1 and the scattering rate becomes proportional to the thickness.

The fact that the intra-subband damping rate decreases as d_1^{-5} for $q_0 d_1 \gg 1$ can be understood as follows: The potential associated with the interface modes decreases exponentially away from interfaces, *i.e.*, $\Phi \propto \exp(-q_0 z)$ for an interface at $z=0$. The matrix element of this potential is estimated as

$$\int_0^{d_1} dz \exp(-q_0 z) \frac{2}{d_1} \sin^2\left(\frac{\pi z}{d_1}\right) \sim \frac{2\pi^2}{d_1^3} \int_0^{\infty} dz \exp(-q_0 z) z^2 \propto \frac{1}{(q_0 d_1)^3}. \tag{3.34}$$

Taking into account an extra factor d_1 arising from the normalization of phonon amplitude, we obtain the desired result $\Gamma_{\eta\eta} \propto d_1^{-5}$.

3-1-4 Envelope-Function Approximation

First, we shall describe briefly how to calculate the eigenmodes in the envelope-function approximation. For modes whose amplitude is dominant in layer l, the reduced envelope in layer l is expanded into sinusoidal curves which have nodes at the layer boundaries as

$$w_{\alpha,l}(z) = \sum_{n_a=1}^{N_a} C_{\alpha,n_a} \sqrt{\frac{2}{d_l}} \sin\left(\frac{n_a \pi}{d_l} z\right) \theta_l(z), \tag{3.35}$$

where N_a is the number of layers of ion pairs in layer l ($N_a = m$ in a $(\mathrm{GaAs})_m(\mathrm{AlAs})_n$ superlattice), C_{α,n_a} is the expansion coefficient, α represents the direction of displacement, and we take $z = 0$ at the left interface. We have introduced a cutoff N_a in order to make the number of the optical modes in this approximation equal to that in the actual superlattices. This cutoff is important only when the layer thickness is small. For simplicity, we do not take the effective layer thickness to be $n+1$ or $n+0.5$ as in Section 2-4 but n, which is a very good

approximation except for superlattices with extremely small layer thickness. The reduced envelope in the other layer l' can be written as

$$w_{\alpha,l'}(z) = \left[C_{A,\alpha} \sqrt{\frac{2q_{\parallel}}{\sinh(q_{\parallel} d_{l'}) - q_{\parallel} d_{l'}}} \sinh[q_{\parallel}(z - d_{l'}/2)] \right. \\ \left. + C_{S,\alpha} \sqrt{\frac{2q_{\parallel}}{\sinh(q_{\parallel} d_{l'}) + q_{\parallel} d_{l'}}} \cosh[q_{\parallel}(z - d_{l'}/2)] \right] \theta_{l'}(z), \tag{3.36}$$

because we employ the dielectric continuum model in this layer, where subscripts S and A denote symmetric and antisymmetric components, respectively.

We assume that the dispersion of phonons is isotropic as given by Eqs. (2.50) and (2.51). In this approximation, there is no mixing of longitudinal and transverse modes. Therefore we can neglect the component of the displacement perpendicular to the wave vector and parallel to layers, because it does not make macroscopic field. Errors arising from this approximation are expected to be small, since the anisotropy has been found to be small in Chap. 2.

Substitution of Eqs. (3.35) and (3.36) into Eq. (2.46) leads to an eigenvalue problem for $2(N_a + 2)$ unknown coefficient C's and phonon frequencies. We normalize the reduced displacement in one period as

$$\int_0^d |\mathbf{w}(z)|^2 dz = 1, \tag{3.37}$$

where $\mathbf{w}(z) = \mathbf{w}_l(z) + \mathbf{w}_{l'}(z)$. Then, the reduced displacement for mode $(j, \mathbf{q})$ at an arbitrary position can be written in a form of second quantization as

$$\mathbf{W}_{j,\mathbf{q}}(\mathbf{r}) = \frac{1}{\sqrt{N}} \sqrt{\frac{\hbar}{2\omega_{j,\mathbf{q}}}} \sum_{n=1}^{N} \mathbf{w}_{j,\mathbf{q}}(z - nd) e^{iq_z nd} \frac{e^{i\mathbf{q}_{\parallel}\cdot\mathbf{r}_{\parallel}}}{L} b_{j,\mathbf{q}} + h.c. \tag{3.38}$$

The electric potential at $\mathbf{r}$ can be written as

$$\Phi_{j,\mathbf{q}}(\mathbf{r}) = \frac{1}{\epsilon_\infty} \int d\mathbf{r}' \frac{\mathbf{P}_{j,\mathbf{q}}(\mathbf{r}') \cdot (\mathbf{r} - \mathbf{r}')}{|\mathbf{r} - \mathbf{r}'|^3}, \tag{3.39}$$

with polarization

$$\mathbf{P}_{j,\mathbf{q}}(\mathbf{r}') = Z(z') e \sqrt{\frac{n}{M(z')}} \mathbf{W}_{j,\mathbf{q}}(\mathbf{r}'), \tag{3.40}$$

where Ze is the effective charge given by Eq. (2.24) and n is the number of cation-anion pairs in a unit volume, *i.e.*, $n = 4/a^3$ for zinc-blende crystals. After some manipulations, the matrix element becomes

$$\begin{aligned} M_{j,\mathbf{q}}(\eta, \eta') &= \int d\mathbf{r} \phi^*_{\eta',\mathbf{k}'}(\mathbf{r}) H_I(\mathbf{r}) \phi_{\eta,\mathbf{k}}(\mathbf{r}) \\ &= \frac{2\pi e^2}{\epsilon_\infty} \frac{1}{\sqrt{N}L} \sqrt{\frac{\hbar}{2\omega_{j,\mathbf{q}}}} \int_0^d dz \int_0^d dz' \\ &\times \left\{ \frac{1}{\exp[(q_{\parallel} - iq_z)d] - 1} \psi^*_{\eta'}(z) \psi_\eta(z) e^{-q_{\parallel}(z-z')} \mathbf{P}_{j,\mathbf{q}}(z') (-i\mathbf{e}_{q_{\parallel}} - \mathbf{e}_z) \right. \\ &+ \frac{1}{\exp[(q_{\parallel} + iq_z)]d - 1} \psi^*_{\eta'}(z) \psi_\eta(z) e^{q_{\parallel}(z-z')} \mathbf{P}_{j,\mathbf{q}}(z') (-i\mathbf{e}_{q_{\parallel}} + \mathbf{e}_z) \\ &\left. + \psi^*_{\eta'}(z) \psi_\eta(z) e^{q_{\parallel}|z-z'|} \mathbf{P}_{j,\mathbf{q}}(z') (-i\mathbf{e}_{q_{\parallel}} + \mathrm{sgn}(z - z')\mathbf{e}_z) \right\} \\ &= -\frac{2\pi e^2}{\epsilon_\infty} \frac{1}{\sqrt{N}L} \sqrt{\frac{\hbar}{2\omega_{j,\mathbf{q}}}} \\ &\times \left\{ \frac{1}{\exp[(q_{\parallel} - iq_z)d] - 1} I_{1,\eta,\eta',l,+} [-iI_{2,x,-} + I_{2,z,-}] \right. \\ &\left. + \frac{1}{\exp[(q_{\parallel} + iq_z)d] - 1} I_{1,\eta,\eta',l,-} [-iI_{2,x,+} + I_{2,z,+}] + I_{3,\eta,\eta',l,x} \right\} \end{aligned} \tag{3.41}$$

where

$$I_{1,\eta,\eta',l,\pm} = \int_0^d dz \psi^*_{\eta'}(z) \psi_\eta(z) e^{\pm q_{\parallel} z} \\ = \begin{cases} \pm \left[(-1)^{\eta+\eta'} e^{\pm q_{\parallel} d_1} - 1 \right] \\ \qquad \times \left\{ \frac{4\eta\eta'\pi^2 (q_{\parallel} d_1)}{[(q_{\parallel} d_1)^2 + \{(\eta+\eta')\pi\}^2][(q_{\parallel} d_1)^2 + \{(\eta-\eta')\pi\}^2]} \right\} & l = 1 \\ \pm e^{\pm q_{\parallel} d_1} \left[(-1)^{\eta+\eta'} e^{\pm q_{\parallel} d_2} - 1 \right] \\ \qquad \times \left\{ \frac{4\eta\eta'\pi^2 (q_{\parallel} d_2)}{[(q_{\parallel} d_2)^2 + \{(\eta+\eta')\pi\}^2][(q_{\parallel} d_2)^2 + \{(\eta-\eta')\pi\}^2]} \right\} & l = 2, \end{cases} \tag{3.42}$$

$$I_{2,\alpha,\pm} = \int_0^d dz' \mathbf{P}_{j,\mathbf{q}}(z') e^{\pm q_{\parallel} z'} (-i\mathbf{e}_{q_{\parallel}} \pm \mathbf{e}_z) \\ = I_{21,\alpha,\pm} + I_{22,\alpha,\pm} \tag{3.43}$$

with

$$I_{21,\alpha,\pm} = Z_l e\sqrt{\frac{n}{M_l}}\sum_n C_{n_a,\alpha}\sqrt{\frac{2}{d_1}}d_1 n_a\pi\frac{1-(-1)^n_a e^{\pm q_{\parallel}d_1}}{(q_{\parallel}d_1)^2+(n_a\pi)^2}, \tag{3.43a}$$

$$\begin{aligned} I_{22,\alpha,\pm} = {} & Z_{l'}e\sqrt{\frac{n}{M_{l'}}}\frac{C_{A,\alpha}}{2q_{\parallel}}\sqrt{\frac{2q_{\parallel}}{\sinh(q_{\parallel}d_2)-q_{\parallel}d_2}}e^{\pm q_{\parallel}(d_1+d_2/2)}\left[\sinh(q_{\parallel}d_2)+q_{\parallel}d_2\right] \\ & \pm Z_{l'}e\sqrt{\frac{n}{M_{l'}}}\frac{C_{S,\alpha}}{2q_{\parallel}}\sqrt{\frac{2q_{\parallel}}{\sinh(q_{\parallel}d_2)+q_{\parallel}d_2}}e^{\pm q_{\parallel}(d_1+d_2/2)}\left[\sinh(q_{\parallel}d_2)-q_{\parallel}d_2\right], \end{aligned} \tag{3.43b}$$

$$\begin{aligned} I_{3,\eta,\eta',l} = {} & I_{1,\eta,\eta',l,+}[-iI_{22,x,-}-I_{22,z,-}] \\ & +Z_l e\sqrt{\frac{n}{M_l}}\sum_n\frac{\sqrt{2d_1}}{(q_{\parallel}d_1)^2+(n\pi)^2}\Big\{n\pi I_{1,\eta,\eta',l,-}[-iC_{n,x}+C_{n,z}] \\ & -n\pi(-1)^n e^{-q_{\parallel}d_1}I_{1,\eta,\eta',l,+}[-iC_{n,x}-C_{n,z}] \\ & -i2q_{\parallel}d_1 I_{S,\eta,\eta',n}-n\pi I_{C,\eta,\eta',n}\Big\}, \end{aligned} \tag{3.44}$$

$$I_{C,\eta,\eta',n} = \begin{cases} -\frac{1}{2} & \text{if } \eta+\eta'-n=0 \\ \frac{1}{2} & \text{if } \eta-\eta'+n=0 \text{ or } \eta-\eta'-n=0 \\ 0 & \text{otherwise,} \end{cases} \tag{3.44a}$$

and

$$I_{S,\eta,\eta',n} = \begin{cases} -\frac{8\eta\eta' n}{\pi[(\eta+\eta')^2-n^2][(\eta-\eta')^2-n^2]} & \eta+\eta'+n\text{: odd} \\ 0 & \text{otherwise.} \end{cases} \tag{3.44b}$$

Damping rates can be calculated numerically using Eq. (3.1). We have not been successful in deriving simple expression for limiting cases for the above equations.

3-2 Numerical Results

3-2-1 Polaron Damping

Figure 2 compares the layer thickness dependence of the polaron damping rate in the GaAs/AlAs superlattices for $d_1 = d_2$ at 300K calculated in the envelope-function approximation, the dielectric continuum model, and the bulk-phonon model. It contains the separate contributions of GaAs-like and AlAs-like modes for the envelope-function approximation and the dielectric continuum model. The

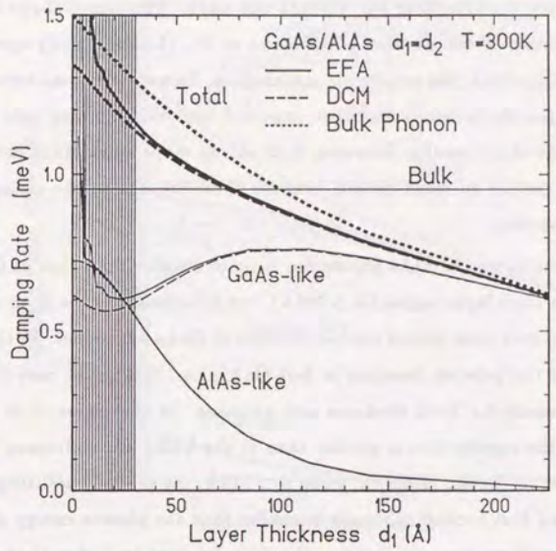

Figure 2 Layer thickness d_1 dependence of the polaron damping rate calculated in the envelope-function approximation (solid line), the dielectric continuum model (dashed line), and the bulk-phonon model(dotted line) at 300K. Thickness of barrier layer d_2 is equal to d_1. For the envelope-function approximation and the dielectric continuum model, the contribution of GaAs-like and AlAs-like modes are also shown. The thin horizontal line represents the damping rate in bulk GaAs. In the hatched region, the assumption that an electron is completely confined to the well layer is invalid.

results of these three models are very similar and increase monotonically with the decrease of the layer thickness. In particular, the result in the dielectric continuum model is almost in agreement with that in the envelope-function approximation.

In the thin layer region ($d_1 < 15$Å), the result in the envelope-function approximation has a zigzag shape and exhibits a sudden increase. This increase is due to lowering of phonon energies by the confinement effect and a resulting increase in phonon number. However, this effect is overestimated, because of the approximation of parabolic phonon dispersion and the assumption that the effective layer

thickness is not $(n+1)a/2$ or $(n+0.5)a/2$ but $na/2$. The zigzag shape is caused by the restriction of the number of modes as in Eq. (3.35). Strictly speaking, in the region of $d_1 < 30$Å, the results are meaningless, because electrons are no longer confined in the GaAs layers and it is expected that the damping rate becomes lower than the above results. However, both zigzag shape and sudden increase are expected to remain to some extent, because these are due to the change in the phonon properties.

The contribution of AlAs-like modes is much smaller than that of GaAs-like modes in the thick layer region ($d_1 > 150$Å), but it increases as the layer thickness decreases and may even exceed the contribution of GaAs-like modes. In this figure, we also show the polaron damping in *bulk* GaAs, *i.e.*, that in the case that there is no confinement for both electrons and phonons. In the region $d_1 > 80$Å, the damping in the superlattice is smaller than in the bulk. The difference increases with the layer thickness. However, when $d_1 > 170$Å, the subband splitting between the lowest and first excited subbands is smaller than the phonon energy and inter-subband transitions strongly increase the damping rate to higher than the bulk value. Hence the reduction of Γ in the superlattice from that in bulk is at most about 20%.

At 77K, Γ is much smaller than at 300K as shown in Fig. 3 because of the decrease of the number $n(\omega)$ of thermally activated phonons [$n(\omega_{LO}) = 0.33$ and 0.17 for GaAs and AlAs, respectively, at 300K and $n(\omega_{LO}) = 4.3\times10^{-3}$ and 5.3×10^{-4}, at 77K.] Note that the difference between Γ calculated in the envelope-function approximation and in the bulk-phonon model is larger than at 300K. This is caused by the reduction of the number of higher energy AlAs-like phonons compared to that of GaAs-like phonons. The difference of Γ between the envelope-function approximation and the dielectric continuum model is also relatively larger than at 300K. This is again due to difference in the phonon number arising from that of phonon energy. Because the reduction of the phonon energy due to confinement is not considered, Γ is underestimated in the dielectric continuum model. The region in which the Γ in superlattices is smaller than that in bulk GaAs extends up to $d_1 > 30$Å.

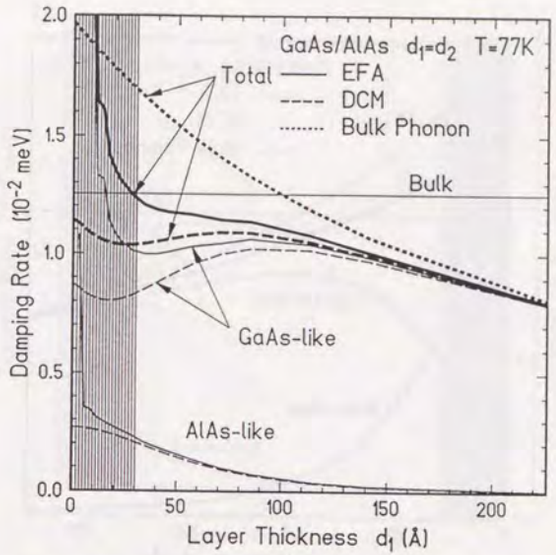

Figure 3 Layer-thickness d_1 dependence of the polaron damping rate at 77K.

In Figs. 4 and 5, we show the results in the case $d_2 = 4d_1$. At 300K, the contribution of the GaAs-like modes is smaller than that in the case $d_2 = d_1$ and the contribution of the AlAs-like modes are larger. Consequently, the total damping rate does not change much. At 77K, the reduction of the damping rate from that in bulk GaAs is slightly more pronounced than for $d_2 = d_1$.

3-2-2 Inter-Subband Relaxation

If the subband splitting is larger than the phonon energy, the following three processes are possible for scattering of an electron at the bottom of the first excited subband:

1) intra-subband transition with phonon absorption,

2) inter-subband transition to the ground subband with phonon absorption,

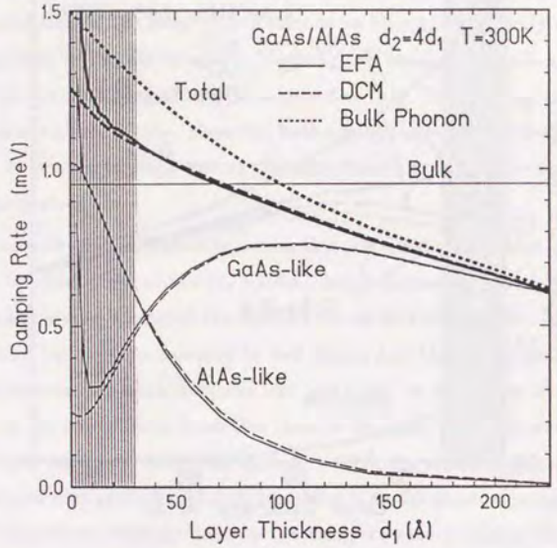

Figure 4 Layer-thickness d_1 dependence of polaron damping rate at 300K. Thickness of barrier layer d_2 is equal to $4d_1$.

3) inter-subband transition to the ground subband with phonon emission.

Figure 6 shows calculated damping rates at 300K as a function of the layer thickness. The damping rate of intra-subband transitions is similar to the polaron damping rate given in Fig. 2. The damping rate for the inter-subband transition with phonon absorption is a sub-linear function of d_1 and that with phonon emission is a super-linear function of d_1, as discussed at the end of Sec. 3-1-2. The results in different approximations are almost indistinguishable for the inter-subband absorption process, while in the emission process the result in the bulk-phonon model is slightly lower. This is due to difference of phonon number $n(\omega)$.

Figure 7 shows calculated damping rates at 77K. The damping rate due to phonon absorption process is smaller by roughly two order of magnitude than at 300K, while that of emission processes remain almost the same.

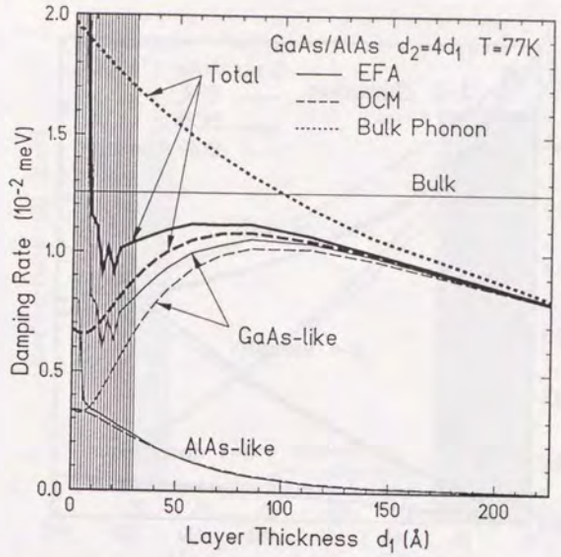

Figure 5 Layer-thickness d_1 dependence of polaron damping rate at 77K. Thickness of the AlAs barrier layer d_2 equals to $4d_1$.

3-3 Discussions

In the preceding section, it has been found that the results in the dielectric continuum model agree quite well with those in the envelope-function approximation and also that even the bulk-phonon model explains the layer thickness dependence reasonably well. In this section, we try to clarify the reason.

For this purpose, we first separate the total scattering rate into contributions of different phonon modes. One way to achieve this separation is to consider the Eliashberg function $\alpha^2(\omega)F(\omega)$ describing the contribution of phonons having frequency ω, defined by

$$\Gamma = \int d\omega \alpha^2(\omega) F(\omega) n(\omega), \tag{3.45}$$

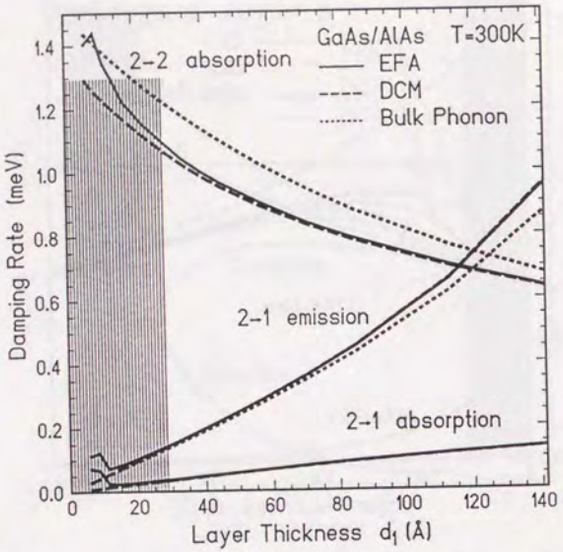

Figure 6 Layer-thickness d_1 dependence of damping rates of an electron at the bottom of the first excited subband, calculated in the envelope-function approximation (solid lines), the dielectric continuum model (dashed lines), and the bulk-phonon model (dotted lines) at 300K. The thickness of the AlAs barrier layer d_2 is equal to d_1.

where $n(\omega)$ is the Planck distribution for phonons, $\alpha(\omega)$ is an effective electron-phonon coupling constant, and $F(\omega)$ is the phonon density of states. For the polaron damping rate, we have from Eq. (3.1)

$$\alpha^2(\omega)F(\omega) = \pi \sum_j \sum_{\mathbf{q}} |M(j,1,1;0,\mathbf{q})|^2 \delta(\omega_j(\mathbf{q}) - \omega)\delta\Big(\frac{\hbar^2 q_{\|}^2}{2m^*} - \hbar\omega\Big). \qquad (3.46)$$

Figure 8 gives the histogram of $\alpha^2(\omega)F(\omega)$ given by

$$E(\omega_n) = \frac{1}{\Delta\omega}\int_{\omega_n}^{\omega_n+\Delta\omega} d\omega \alpha^2(\omega)F(\omega) \qquad (3.47)$$

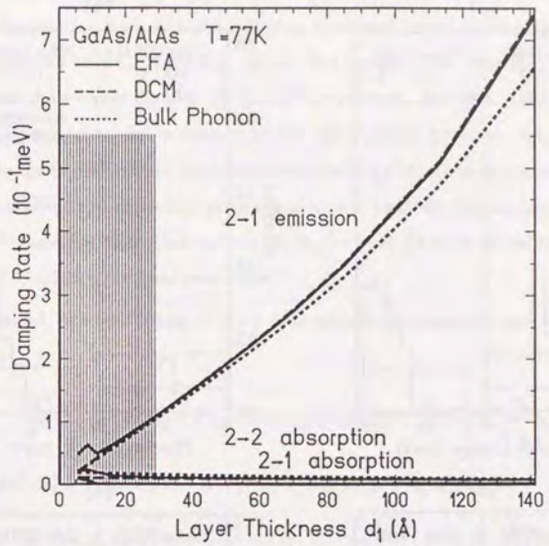

Figure 7 Layer-thickness d_1 dependence of damping rate of an electron at the bottom of the first excited subband at 77K. The contribution of inter-subband transition due to phonon emission is much larger than those of other two processes.

with $\omega_n = n\Delta\omega$ for GaAs/AlAs superlattices with $d_1 = d_2 = 28$ Å and $d_1 = d_2 = 113$ Å. For $d_1 = d_2 = 113$ Å, the histograms calculated in the envelope-function approximation and the dielectric continuum model are quite similar. This shows that the dielectric continuum model is accurate in superlattices with wide layers. For $d_1 = d_2 = 28$ Å, the histograms with $\Delta\omega = 1$ meV differ between the envelope-function approximation and the dielectric continuum model, showing that the latter breaks down for narrow layers, while those with $\Delta\omega = 10$ meV do not. This suggests that the total scattering rate is not sensitive to the details of the model even though differential contributions of individual modes are quite different. This approximate model independence can be demonstrated analytically.

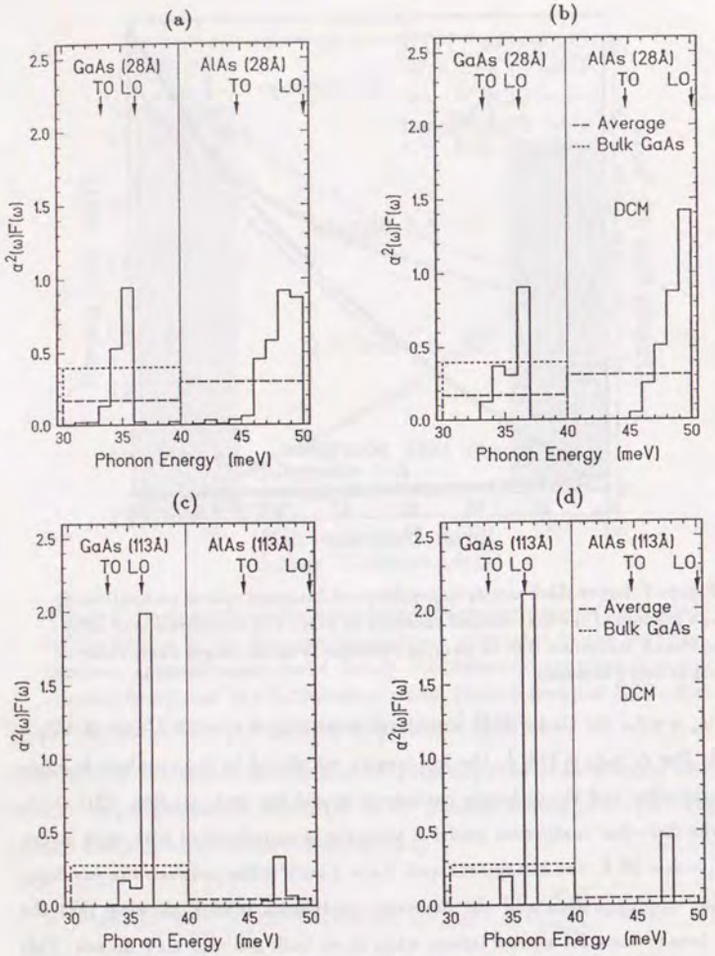

Figure 8 Histogram of the Eliashberg function for the polaron damping rate in a $(GaAs)_{10}(AlAs)_{10}$ superlattice calculated in the envelope-function approximation (a) and the dielectric continuum model (b) and in a $(GaAs)_{40}(AlAs)_{40}$ superlattice in the envelope-function approximation (c) and the dielectric continuum model (d). The solid lines show the result when the frequency interval is 1 meV and the dashed lines 10 meV. The dotted lines represent the result in the bulk-phonon model

Before proceeding further, we should note that the sum of the contributions of GaAs-like modes and AlAs-like modes is almost equal to that calculated in the bulk-phonon model. Actually, this is the reason that even the bulk-phonon model gives reasonable results. It should be noticed, however, that the validity of the bulk-phonon model is limited to the GaAs/AlAs systems. The situation is likely to be quite different in superlattices consisting of other materials. Mori and Ando[3] showed in the dielectric continuum model that the scattering rate can be considerably smaller than that calculated in the bulk-phonon model in AlSb/InAs /AlSb and Ge/InAs/Ge quantum wells.

In general, the scattering rate by optical-phonon emission and absorption is written as

$$\frac{1}{\tau_{\eta,\eta',\pm}} = \frac{2\pi e^2}{\hbar}\sum_j\sum_{\mathbf{q}}\delta\big(E_i - E_f \pm \hbar\omega_j(\mathbf{q})\big)\big[n(\omega_{j,\mathbf{q}}) + \frac{1}{2} \pm \frac{1}{2}\big]\big(\frac{\hbar}{2\omega_{j,\mathbf{q}}}\big)$$
$$\times \int d\mathbf{r}_1^3 d\mathbf{r}_1'^3 d\mathbf{r}_2^3 d\mathbf{r}_2'^3 \psi^*_{\eta'}(\mathbf{r}_1,\mathbf{k}+\mathbf{q})\psi_{\eta}(\mathbf{r}_1,\mathbf{k})\psi_{\eta'}(\mathbf{r}_2,\mathbf{k}+\mathbf{q})\psi^*_{\eta}(\mathbf{r}_2,\mathbf{k})$$
$$\times K(\mathbf{r}_1,\mathbf{r}_1')K^*(\mathbf{r}_2,\mathbf{r}_2')Z(\mathbf{r}_1')e\sqrt{\frac{n}{M(\mathbf{r}_1')}}Z(\mathbf{r}_2')e\sqrt{\frac{n}{M(\mathbf{r}_2')}}\big(\mathrm{div}_{\mathbf{r}_1'}\mathrm{div}_{\mathbf{r}_2'}\big)\big(\mathbf{W}_{j,\mathbf{q}}(\mathbf{r}_1')\mathbf{W}^*_{j,\mathbf{q}}(\mathbf{r}_2')\big), \tag{3.48}$$

where $K(\mathbf{r},\mathbf{r}')$ is a kernel which determines the potential at $\mathbf{r}$ for a unit charge density at $\mathbf{r}'$. When ε_∞ is independent of the constituent materials, we have

$$K(\mathbf{r},\mathbf{r}') = \frac{1}{\epsilon_\infty|\mathbf{r}-\mathbf{r}'|}. \tag{3.49}$$

When ε_∞ varies between layers, the kernel becomes far more complicated because of image charge effects.

Let us assume that the frequencies of all optical modes are about the same and can be replaced by an averaged frequency ω_{AV}. Because the energy of an electron is independent of k_z, $\mathbf{q}_{||}$ is determined as $|\mathbf{q}_{||}| = \sqrt{q_x^2+q_y^2} = q_0$ to satisfy the energy conservation and q_z is arbitrary. Because $\mathbf{W}_{j,\mathbf{q}}(\mathbf{r})$ ($\propto e^{i\mathbf{q}_{||}\cdot\mathbf{r}_{||}}$) is a solution of an integro-differential equation for each $\mathbf{q}$, we have the closure relation

$$\sum_j\sum_{q_z} W_{\alpha,j,\mathbf{q}}(\mathbf{r})W^*_{\beta,j,\mathbf{q}}(\mathbf{r}') = \delta_{\alpha,\beta}\delta(z-z')\frac{\exp[i\mathbf{q}_{||}\cdot(\mathbf{r}_{||}-\mathbf{r}'_{||})]}{L^2}, \tag{3.50}$$

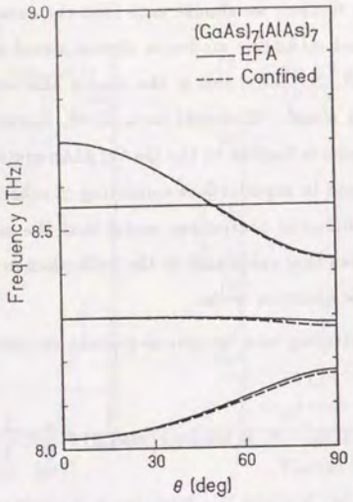

Figure 9 Dependence of the frequency of modes lying in the vicinity of the LO and TO phonons of GaAs on the wave vector direction at the Γ point. The solid lines represent the results calculated in the envelope-function approximation and the dashed lines those of the confined model described in the text. The results in the envelope-function approximation are the same as those given in Fig. 11(a) of Chap. 2.

where $\alpha, \beta = x, y, z$. Therefore, the summation over j and q_z gives

$$\begin{aligned}\frac{1}{\tau_{\eta,\eta',\pm}} = \frac{2\pi e^2}{\hbar}\sum_{q_x,q_y}\frac{m^*}{q_{0,AV}\hbar}\delta(q_{\|}-q_{0,AV})\Big[n(\omega_{AV})+\frac{1}{2}\pm\frac{1}{2}\Big]\Big(\frac{\hbar}{2\omega_{AV}}\Big)\\ \times\int dr_1^3\int dr_1'^3\int dr_2^3\int dr_2'^3\Big[\psi^*_{\eta',\mathbf{k}+\mathbf{q}}(\mathbf{r}_1)\psi_{\eta,\mathbf{k}}(\mathbf{r}_1)\psi_{\eta',\mathbf{k}+\mathbf{q}}(\mathbf{r}_2)\psi^*_{\eta,\mathbf{k}}(\mathbf{r}_2)\\ \times K(\mathbf{r}_1,\mathbf{r}_1')K^*(\mathbf{r}_2,\mathbf{r}_2')Z(\mathbf{r}_1')e\sqrt{\frac{n}{M(\mathbf{r}_1')}}Z(\mathbf{r}_2')e\sqrt{\frac{n}{M(\mathbf{r}_2')}}\\ \times\big(\mathrm{div}_{(\mathbf{r}_1')}\mathrm{div}_{(\mathbf{r}_2')}\big)\Big(E\delta(z_1'-z_2')\frac{\exp[i\mathbf{q}_{\|}(\mathbf{r}_{1,\|}'-\mathbf{r}_{2,\|}')]}{L^2}\Big)\Big],\end{aligned} \tag{3.51}$$

where E is a 3×3 unit matrix. This shows that the scattering rate does not depend on the details of the displacement of each phonon mode.

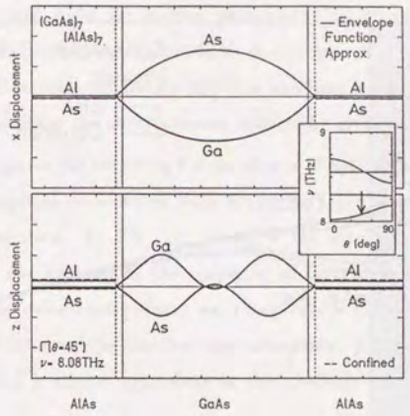

Figure 10 Calculated displacements of ions for a mode at the Γ point and the wave vector direction $\theta=\pi/4$. $\nu=8.08$THz. The solid lines represent results calculated in the envelope-function approximation and the dashed lines represent those in the confined model described in the text. The thin vertical straight lines indicate the position of interfacial As planes and the vertical dotted lines the interface position in the envelope-function approximation. The results in the envelope-function approximation are the same as those given in Fig. 12(b) of Chap. 2.

This sum rule corresponds to that noted by Mori and Ando.[3] They investigated the polaron damping rate in single and double heterostructures in the dielectric continuum model. The damping rate has been expressed as

$$\Gamma \cong \frac{\pi}{2}\sum_j \mathcal{A}_j(q_{0,j})\omega_j(q_{0,j})n\big(\omega_j(q_{0,j})\big)\mathcal{F}_j(q_{0,j}), \tag{3.52}$$

where j is the mode index, $q_{0,j}$ is the norm of the two-dimensional wave vector for which the energy conservation is satisfied, $\mathcal{A}_j$ is the coupling constant of mode j, and $\mathcal{F}_j$ is a form factor. In the case of l-like modes, $\mathcal{A}_j = \alpha_{F,l}$ if $\omega_j = \omega_{LO,l}$ and $\mathcal{A}_j = 0$ if $\omega_j = \omega_{TO,l}$.[3] They found that the form factors obey a sum rule,

$$\mathcal{F}_B(\mathbf{q}_{\|}) = \sum_j \mathcal{F}_j(\mathbf{q}_{\|}) \tag{3.53}$$

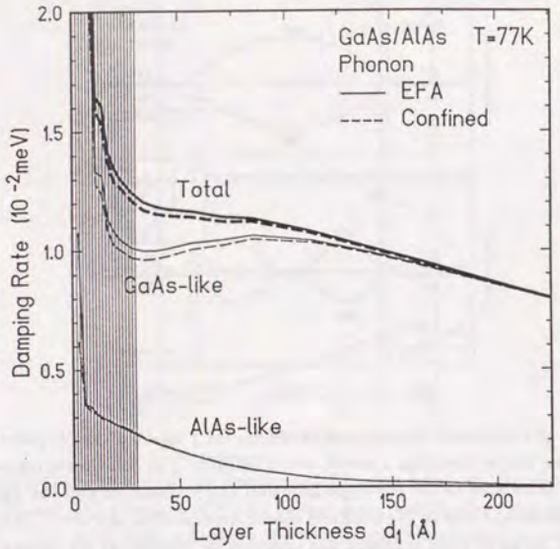

Figure 11 Layer-thickness d_1 dependence of polaron damping rate calculated in the confined model (solid lines) and the envelope-function approximation (dashed lines) at 77K. Thickness of the AlAs barrier layer d_2 is equal to d_1. The results in the envelope-function approximation is the same as those given in Fig. 3.

where $\mathbf{q}_{||}$ is two-dimensional wave vector and $\mathcal{F}_B$ is the form factor of the bulk-phonon model. This sum rule is a direct consequence of the completeness of the phonon modes shown above and means that as long as $\mathcal{A}_j\omega_j n$ is almost independent of j, the damping rate is close to that in the bulk-phonon model. This condition is approximately satisfied for GaAs/AlAs systems. This is the reason why the bulk-phonon model explains the layer thickness dependence reasonably well. However, this sum rule alone does not explain the reason why the results in the dielectric continuum model agree so well with those in the envelope-function approximation.

Figure 8 shows that α^2F averaged over GaAs-like modes and over AlAs-like modes in the envelope-function approximation and the dielectric continuum model

are in good agreement. This suggests the presence of a completeness relation for GaAs-like modes and AlAs-like modes, separately. To prove this, we consider a model in which the displacement is confined to one type of layers (say l) and where the other layer l' is replaced by an effective medium having dielectric constant $\epsilon_{l'}(\omega_{LO,l})$. This satisfies the completeness within the layer l.

Figure 9 compares the resulting θ dependence of optical modes with frequency close to that of optical phonons in bulk GaAs with the results in the envelope-function approximation. In Fig. 10, we show the displacement for a mode at $\theta = \pi/2$, where the amount of the response of layer l' is reinterpreted as the displacement. The calculated polaron damping rate is shown in Fig. 11 together with the result of the envelope-function approximation. All these figures show that this confined model is almost equivalent to the envelope-function approximation.

We can immediately derive an expression of the relaxation time similar to that given by Eq. (3.51) except that the kernel K should be replaced by that corresponding to the confined model and $\delta(z_1'-z_2')$ should be replaced by $\delta(z_1'-z_2')\theta_l(z_1')$. Therefore, the total contribution of GaAs or AlAs like modes is independent of the details of each mode as long as its frequency can approximately be replaced by a certain average value. The same is applicable to the dielectric continuum model, since a similar confined model is equally valid. This explains why the dielectric continuum model is successful in giving the electron scattering rate even in superlattices with narrow layers although it cannot describe each phonon modes correctly.

It should be noted that the near equivalence between the envelope-function approximation and the simpler confined model is limited to the GaAs/AlAs systems, where $|\omega_{\rm LO}^{\rm GaAs}-\omega_{\rm TO}^{\rm GaAs}| \ll |\omega_{\rm LO}^{\rm AlAs}-\omega_{\rm LO}^{\rm GaAs}|$ and $|\omega_{\rm LO}^{\rm AlAs}-\omega_{\rm TO}^{\rm AlAs}| \ll |\omega_{\rm LO}^{\rm AlAs}-\omega_{\rm LO}^{\rm GaAs}|$, *i.e.*, the difference between the LO and TO frequencies of each material is smaller than the difference in the LO or TO frequencies of two materials. The envelope-function approximation is not subject to such limitations and has a wider applicability than the confined model.

The present calculations show that the electron-optical phonon interaction becomes stronger as the layer thickness decreases. Opposite results were obtained

by some authors. In particular, Riddoch and Ridley[4] calculated the scattering rate of electrons confined in a thin ionic slab, using the dielectric continuum model, and showed that it decreases as the layer thickness decreases. We can obtain similar result if we neglect contributions from adjacent AlAs layers. Sawaki[5] calculated the scattering rate, assuming that the optical phonons are completely confined in either layer and the amplitude of displacement is described by sinusoidal curves vanishing at the interfaces. The calculated intra-subband scattering rate again decreases as the layer width decreases. The present study shows that the underlying assumption of his calculation is incorrect.

In actual experiments, we observe the damping of an electron in the presence of many other electrons. Thus the so-called many-body effects might alter the present conclusion. Among them, the Pauli principle and the screening to the electron-phonon interaction are the two important effects to be considered. The Pauli principle can affect the damping rate at temperatures below the Fermi energy. However, in the high-temperature region of our interest, we can ignore this effect safely.[1] The screening effect can also be neglected, because it is quantitatively small as investigated by Mason and Das Sarma.[1] They showed that the damping rate due to phonon absorption is reduced by the static screening effect to at most 70% of the unscreened result at $T = 300$K in a single quantum well with thickness $d_1 = 100$Å and electron sheet density $N_S = 3 \times 10^{11}\text{cm}^{-2}$. Actually, the screening process comes into play as a dynamical rather than a static one. In the dynamical screening, its effect is reduced further as evaluated by Das Sarma *et al.*[6] According to their calculation, the damping rate with the dynamically screened electron-phonon interaction is close to the one without the screening at low N_S.

References

1. B.A. Mason and S. Das Sarma, Phys. Rev. B **35**, 3890 (1987).
2. P.J. Price, Phys. Rev. B **30**, 2234 (1984).
3. N. Mori and T. Ando, Phys. Rev. B **40**, 6175 (1989).
4. F.A. Riddoch and B.K. Ridley, Physica **134B**, 342 (1985).
5. N. Sawaki, J. Phys. C **19**, 4965 (1986).
6. S. Das Sarma, A. Kobayashi, and W.Y. Lai, Phys. Rev. B **36**, 8151 (1987).

Chapter 4

Summary

In this thesis, I have investigated the behavior of phonons and the electron–optical-phonon interactions in semiconductor superlattices, mainly in GaAs/AlAs superlattices which have been most extensively studied up to now.

In Sec. 2.1, I give a brief review on some simple models of phonons in superlattices: the linear-chain model, the elastic continuum model, and the dielectric continuum model. The linear-chain model and the dielectric continuum model give different results for the optical phonons in GaAs/AlAs superlattices. In the linear-chain model, all optical modes are confined in either layer and the displacement has nodes at the interfaces. It is applicable only for wave vectors perpendicular to the layers. In the dielectric continuum model, there are four modes which are not confined in either layer and have frequencies dependent on the direction of wave vector at the Γ point and the maximum displacement at interfaces. For modes confined in either layer, the perpendicular component of displacement has maxima at interfaces.

In Secs. 2-2 and 2-3, I investigate the behavior of phonons in a GaAs/AlAs superlattice by lattice dynamics. I employ the valence-force field model characterized by two short-range force constants C_0 and C_1 and a fixed effective charge Z which takes care of the long-range Coulomb interaction. The overall feature of the spectra, *i.e.*, the confinement of optical modes and the folding of acoustic modes in reciprocal space, is consistent with the results already obtained by linear-chain

models. There exists an important modification due to the long-range Coulomb force, however. It causes a large anisotropy in the dispersion of optical phonons in the vicinity of the Γ point and gives rise to Fuchs-Kliewer or interface modes which have nonvanishing amplitudes in both GaAs and AlAs layers. It has also been shown that the tetrahedral bond structure supports characteristic interface modes at the transverse X points.

All features mentioned above cannot be reproduced by either the linear-chain model or the dielectric continuum model alone. An envelope-function approximation for long wavelength optical phonons in superlattices is developed in Sec. 2-4. In this approximation, displacement is approximated by the envelope which has nodes at appropriate boundary planes. For the modes for which mainly the atoms in the GaAs-layer oscillate, dispersion of phonons in bulk-GaAs is approximated by a 3×3 matrix Hamiltonian and that in bulk AlAs is ignored, and vice versa. The results in this approximation reproduce both frequencies and displacements quite well. This approximation can be applicable to all problems related to electron–optical-phonon interactions in superlattices.

Calculations have been extended to GaSb/AlSb and GaP/AlP superlattices. In the former system, the optical phonons of the constituent materials are completely separated from each other and the phonon spectra are similar to those of GaAs/AlAs superlattices. In the GaP/AlP system, on the other hand, the ω_{LO} and ω_{TO} of GaP lie above the LO and TO frequencies of AlP in the vicinity of X points. Therefore, some of confined optical phonons of GaP, especially LO phonons, are mixed with LO phonons in AlP layers and the phonon spectrum becomes quite complicated. The envelope-function approximation fails to reproduce some of such modes.

In Chapter 3, electron–optical-phonon interaction in GaAs/AlAs superlattices have been investigated. Methods of calculation have been shown in Sec. 3-1, in the bulk-phonon model, the dielectric continuum model, and our envelope-function approximation. In Sec. 3-2, I have numerically calculated the polaron damping and inter-subband relaxation rates as a function of layer thickness. At 300K, the polaron damping increases monotonically as the layer thickness decreases and

the damping is lower than that in bulk GaAs above 80Å. Quite different from at 300K, the damping at 77K depends only weekly on layer thickness when < 100Å. The inter-subband relaxation rates increase almost linearly as the layer thickness increases. At 77K, the phonon emission process is dominant. It has been found that the results in the dielectric continuum model agree quite well with those in the envelope-function approximation and that even the bulk-phonon model explains the layer thickness dependence reasonably well.

In Sec. 3-3, the Eliashberg function is defined and calculated in order to investigate explicitly to what extent individual modes contribute to the electron scattering. It shows that the dielectric continuum model is quite accurate in superlattices with wide layers but fails to describe individual modes for narrow layers. This means that contributions of individual modes are quite different although the total scattering rate is the same. This approximate model-independence of the total scattering rate is understood in terms of the completeness of the phonon modes. As a matter of fact, the global completeness of all modes in GaAs and AlAs layers explains why the bulk-phonon model can give a reasonable layer-thickness dependence. A simpler model is introduced in which displacements are totally confined in either GaAs or AlAs layers and other layers are replaced by a continuum having an appropriate dielectric constant independent of frequency. Its approximate validity is established by comparison with frequencies and displacements calculated in the envelope-function approximation. The completeness within this confined model explains why the dielectric continuum model gives accurate total scattering rates for both GaAs and AlAs like modes even in thin-layer superlattices.

Appendix A

Convenient Method for the Linear-Chain Model[1]

The equations of motion for the four atoms at the interfaces are

$$\begin{aligned}
M_c'\frac{d^2u_c'(0)}{dt^2} &= f_1[u_a'(0)-u_c'(0)]+f_2[u_a(l-1)-u_c'(0)],\\
M_a\frac{d^2u_a(l-1)}{dt^2} &= f_1[u_c(l-1)-u_a(l-1)]+f_2[u_c'(0)-u_a(l-1)],\\
M_c\frac{d^2u_c(0)}{dt^2} &= f_1[u_a'(0)-u_c'(0)]+f_2[u_a'(l-1)e^{-ikd}-u_c(0)],\\
M_a'\frac{d^2u_a'(m-1)e^{-ikd}}{dt^2} &= f_1[u_c'(m-1)-u_a'(m-1)]e^{-ikd}\\
&\quad +f_2[u_c(0)-u_a'(m-1)e^{-ikd}],
\end{aligned} \tag{A.1}$$

where u_c and u_a are the displacements of an anion and a cation in layer 1, u_c' and u_a' are those in layer 2, M_c and M_a are the masses of an anion and a cation in layer 1, M_c' and M_a' are ones in layer 2, d is the period of this superlattice, k is the wave vector, and we assumed $f_1 = f_1'$ and $f_2 = f_2' = f_i = f_i'$ for simplicity. Extrapolating the bulk displacement, we obtain

$$\begin{aligned}
M_c'\frac{d^2u_c'(0)}{dt^2} &= f_1[u_a'(0)-u_c'(0)]+f_2[u_a'(-1)-u_c'(0)],\\
M_a\frac{d^2u_a(l-1)}{dt^2} &= f_1[u_c(l-1)-u_a(l-1)]+f_2[u_c(l)-u_a(l-1)],\\
M_c\frac{d^2u_c(0)}{dt^2} &= f_1[u_a(0)-u_c(0)]+f_2[u_a(-1)e^{-ikd}-u_c(0)],\\
M_a'\frac{d^2u_a'(m-1)e^{-ikd}}{dt^2} &= f_1[u_c'(m-1)-u_a'(m-1)]e^{-ikd}\\
&\quad +f_2[u_c'(m)-u_a'(m-1)]e^{-ikd}.
\end{aligned} \tag{A.2}$$

Subtracting Eqs. (A.1) from (A.2), we get

$$\begin{aligned}
&u_c(l)-u_c'(0)=0,\\
&u_c(0)-u_c'(m)e^{-ikd}=0,\\
&u_a(l-1)-u_a'(-1)=0,\\
&u_a(-1)-u_a'(m-1)e^{-ikd}=0.
\end{aligned} \tag{A.3}$$

The solution can generally be written as

$$\begin{aligned} u_c(s) &= Ae^{iqa_0 s} + Be^{-iqa_0 s}, \\ u_c'(s) &= A'e^{iq'a_0 s} + B'e^{-iq'a_0 s}, \\ u_a(s) &= A\gamma_+ e^{iqa_0 s} + B\gamma_- e^{-iqa_0 s}, \\ u_a'(s) &= A'\gamma_+' e^{iq'a_0 s} + B'\gamma_-' e^{-iq'a_0 s}, \end{aligned} \tag{A.4}$$

where q and q' are local wave vector with in layer 1 and 2, respectively, A,B,A', and B' are coefficients to be determined, $a_0 = a/2$, and

$$\gamma_\pm = \frac{u_a}{u_c} = \frac{f_1 + f_2 e^{\pm iqa_0}}{(f_1 + f_2) - M_a\omega^2}. \tag{A.5}$$

Substituting Eqs. (A.4) into Eq. (A.3), we obtain the secular equation

$$\begin{vmatrix} e^{iqa_0 l} & e^{-iqa_0 l} & -1 & -1 \\ 1 & 1 & -e^{iq'a_0 m}e^{-ikd} & -e^{-iq'a_0 m}e^{-ikd} \\ \gamma_+ e^{iqa_0(l-1)} & \gamma_- e^{-iqa_0(l-1)} & -\gamma_+' e^{-iq'a_0} & -\gamma_-' e^{iq'a_0} \\ \gamma_+ e^{-iqa_0} & \gamma_- e^{iqa_0} & -\gamma_+' e^{iq'a_0(m-1)}e^{-ikd} & -\gamma_-' e^{-iq'a_0(m-1)}e^{-ikd} \end{vmatrix} = 0, \tag{A.6}$$

which has solutions for

$$\cos(kd) = \cos(\bar{q}d) + \eta \sin(qd_1)\sin(q'd_2), \tag{A.7a}$$

with

$$\bar{q} = \frac{qd_1 + q'd_2}{d_1 + d_2}, \tag{A.7b}$$

$$\eta = \frac{2(G_+G_- + G_+'G_-')}{G_+G_+' + G_-G_-' - G_+G_-' - G_-G_+'}, \tag{A.7c}$$

where $d_1 = la_0$ is the thickness of layer 1, $d_2 = ma_0$ is the thickness of layer 2, $\bar{q}$ is an averaged wave vector, and

$$G_\pm = \gamma_\pm e^{\mp iqa_0}. \tag{A.8}$$

Eq. (A.7a) is very similar to eigenvalue conditions for electrons in periodic square potential wells, *i.e.* , the Kronig-Penney model.

Reference

1. B. Jusserand, D. Paquet, A. Regreny, and J. Kervarec, J. Phys. (Paris) Colloq., **45**, C5-145(1984).

Appendix B

Boundary Condition on Lattice Displacement[1]

From the equation of motion for the interfacial As and Al atoms, we obtain a relation by similar procedure in Appendix A:

$$\begin{aligned} u_{a,A}(n+1) &= u_{a,B}(n+1) \quad \text{at } z = -a_0/2, \\ u_{c,A}(n+2) &= u_{c,B}(n+2) \quad \text{at } z = a_0/2, \end{aligned} \tag{B.1}$$

where subscripts a and c denote anion and cation and A and B denote GaAs and AlAs, respectively, and $a_0 = a/4$. In case of longitudinal modes, the displacements in the GaAs layer are

$$\begin{aligned} u_{a,A}(n+1) &= -\frac{M_{Ga}}{M_{Ga}+M_{As}} u\Big(-\frac{a_0}{2}\Big), \\ u_{c,A}(n+2) &= \frac{M_{As}}{M_{Ga}+M_{As}} u\Big(\frac{a_0}{2}\Big), \end{aligned} \tag{B.2}$$

where $u(z)$ is the envelope function. On the other hand, the displacement in the AlAs layers are given by a linear combination of an evanescent mode χ and a mode ψ induced by a macroscopic electric field as

$$\begin{aligned} u_{a,B}(n+1) &= \chi_{As} + \psi_{As}, \\ u_{c,B}(n+2) &= \chi_{Al} + \psi_{Al}, \end{aligned} \tag{B.3}$$

where $\psi_{Al}/\psi_{As} = -(M_{As}/M_{Al})(E_{Al}/E_{As})$ with macroscopic electric field E_{As} and E_{Al} at interfacial As and Al plane, respectively. Using the above equation and Taylor expansion $u(\epsilon) = u(0) + \epsilon \Delta u$, we have

$$u(z_0) = f_\psi \tag{B.4}$$

with

$$\begin{aligned} f_\psi &= \frac{1 + M_{Ga}/M_{As}}{\alpha + M_{Ga}/M_{As}} (\alpha\psi_{Al} - \psi_{As}) \\ z_0 &= \frac{\alpha - M_{Ga}/M_{As}}{\alpha + M_{Ga}/M_{As}} \Big(\frac{a_0}{2}\Big), \end{aligned} \tag{B.5}$$

where z_0 is the place where χ vanishes and $\alpha = \chi_{As}/\chi_{Al}$ at the TO frequency of bulk GaAs is shown to be 0.77 by the lattice dynamics in bulk AlAs. Usually, the displacement in the AlAs layer, ψ, due to a macroscopic field is quite small compared to that in the GaAs layer. Therefore, Eq. (B.5) lead to the boundary condition that the envelope vanishes at $z_0 = -0.05a_0$, *i.e.* close to the midpoint between the interfacial As and Al planes. Similar boundary conditions can be obtained for GaAs-like TO modes and for AlAs-like modes. When these results are applied to a $(GaAs)_n(AlAs)_m$ superlattice, the effective thickness in the case of GaAs-like optical phonons is d(GaAs,LO)=$(n + 0.5)a/2$ for longitudinal and d(GaAs,TO)=$(n + 0.8)a/2$ for transverse modes. In the case of AlAs-like optical phonons, on the other hand, it is d(AlAs,LO)=$(n + 1.1)a/2$ for longitudinal and d(AlAs,TO)=$(n + 1.0)a/2$ for transverse modes. These values are in good agreement with the results obtained in Sec. 2-3-1.

Reference

1. H. Akera and T. Ando, Phys. Rev. B40, 2914(1989).